Study of $B \to \pi l \bar{\nu}$ semileptonic decay using lattice nonrelativistic QCD

Hideo Matsufuru

Department of Physics, Hiroshima University

Thesis, March 1998

Contents

1 INTRODUCTION

1.1 Lattice B Physics

Study of the B meson systems, which contain single b-quark (mass $m_b \sim 4.1$–$4.5\ GeV$), is referred as B physics, and is one of the most important subjects of current particle physics. In the framework of the standard model, weak decays of B mesons are governed by the Cabibbo-Kobayashi-Maskawa (CKM) matrix, the unitary matrix which causes the mixing among quark generations [1, 2]. Thus precise measurements of the CKM matrix elements are necessary to test a validity of the standard model and to search a new physics beyond the standard model [3]. Detection of CP violation in $B\bar{B}$ system will give us detailed information on the complex phases of the CKM matrix, which would shed light on the baryon asymmetry problem of the universe [3]. For this aim, B Factories, dedicated accelerators to study B decay modes, are under construction and will start to work near future [4].

To extract the CKM matrix element precisely from experimental data, it is crucial to evaluate relevant hadronic matrix elements which suffer nonperturbative effect of the quantum chromodynamics (QCD). On this point, recent progress of the heavy quark effective theory (HQET) has much proceeded the understanding of the dynamics of the heavy-light systems [6]. However there still remains large uncertainties, since the HQET predicts only relations among the matrix elements. The lattice simulation enables us evaluation of these matrix elements incorporating the nonperturbative effect from the first principle. In fact, much effort has been payed for the lattice studies of the weak matrix elements, as well as the mass spectrum and the decay constants of B mesons. For example, on the decay constant of B meson, f_B, current lattice results in the quenched approximation agree within 20 %, and successive works with and without the dynamical quarks will give more reliable answer [14]. On the other hand, calculation of the semileptonic form factors still remains a challenging subject, and requires more works with development of computational procedures [12, 13, 14]. This work deals with a lattice calculation of the hadronic matrix element of the semileptonic weak decay $B \to \pi l \bar{\nu}$ (Fig. 1).

In principle, lattice simulations can compute any hadronic matrix elements from the first principle. There is, however, a problem in treating a heavy quark with mass m_Q on the lattice with currently available computer power. A typical lattice cutoff accessible in current simulations, $a^{-1} \sim 1 - 3\ GeV$, is much less than the b-quark mass, $m_b \sim 4\ GeV$. This causes unacceptably large systematic errors of order of am_Q. Thus the early lattice calculations of the B systems using the standard Wilson or clover actions involved an extrapolation in the heavy quark mass from the charm quark mass regime

Figure 1: Semileptonic decay process $B \to \pi l \bar{\nu}$.

to the b-quark mass assuming a heavy quark mass scaling law, which could introduce a potential systematic error. An alternative approach is to use effective theories, such as the nonrelativistic QCD [24] and the Fermilab action [35], in which large mass scale of order m_Q is removed from the dynamics. These theories are not models but the systematic expansions of the original QCD in a sense that one can reproduce the same results as in QCD within a given order of, *e.g.* $1/m_Q$ in NRQCD. In this work, we use the lattice nonrelativistic QCD (NRQCD) up to $O(1/m_Q)$ corrections, thus it enables direct simulations at the physical b-quark mass.

As an calculation of the weak decay form factors, this work is the first application of NRQCD. As mentioned above, previous calculations involve an extrapolation from the charm quark region to the B meson scale with a help of HQET scaling law. Since this extrapolation leads potential uncertainties, direct simulation on the b-quark mass is required to study the matrix element in detail. One of the goals of this exploratory study is to test an applicability of NRQCD to these semileptonic processes and to clarify the problems which should be considered in future calculations with higher statistics and improvements. The procedures used in this work is easily applicable to calculations of other processes, such as $B \to \rho$ and $B \to K^*$, which should also play important roles in future B physics.

This thesis is organized as follows. The rest of this section contains a brief survey of theoretical ideas concerning $B \to \pi$ decays, and current lattice works on this process. In the next section, we summarize the NRQCD formulation and numerical method to calculate the matrix elements. The details of our numerical simulation is described in

Section 3. There we point out the subtleties in extracting the form factors: the definition of the heavy meson energy, the choice of the two independent matrix elements to determine f^+ and f^0, and the procedure of chiral extrapolation. We study the uncertainties due to the extraction and explain what is the best procedure. Physical implications of numerical results are discussed in Section 4. We study $1/m_B$ dependence of the matrix elements and q^2 dependence of the form factors. The prediction from the soft pion theorem is compared with our data. In Section 5, we examine the systematic uncertainties contained in this work. Section 6 is devoted to our conclusion.

1.2 B meson decays and basic theoretical ideas

In this subsection we briefly summarize basic quantities and notions in B physics. We also include ideas of heavy quark effective theory and heavy meson effective theory in this subsection for later use.

Form factors The hadronic matrix elements of the $B \to \pi$ semileptonic decay are expressed in terms of two form factors f^+ and f^0 as

$$\langle \pi(\boldsymbol{k})|V_\mu|B(\boldsymbol{p})\rangle = \left(p + k - q\frac{m_B^2 - m_\pi^2}{q^2}\right)_\mu f^+(q^2) + q_\mu \frac{m_B^2 - m_\pi^2}{q^2} f^0(q^2), \tag{1}$$

where $q_\mu = p_\mu - k_\mu$. These two form factors correspond to the scalar and the vector particles exchange modes respectively. The covariant normalization of the meson fields is employed in this paper:

$$\langle M(\boldsymbol{p}')|M(\boldsymbol{p})\rangle = 2p_0(2\pi)^3\delta^3(\boldsymbol{p} - \boldsymbol{p}'). \tag{2}$$

From the condition that the matrix element is not singular at $q^2 = 0$, the form factors satisfy $f^+(0) = f^0(0)$. The kinematical end point $q^2_{\rm max} = (m_B - m_\pi)^2$ corresponds to the zero recoil limit, where the lattice simulation works most efficiently.

For the massless lepton cases, $f^+(q^2)$ dominates the decay rate, so that

$$\frac{d\Gamma(\bar{B}^0 \to \pi^+ l\bar{\nu})}{dq^2} = \frac{G_F^2}{192\pi^3 m_B^3}\lambda^{3/2}(q^2)\,|V_{ub}|^2|f^+(q^2)|^2, \tag{3}$$

where V_{ub} is the Cabibbo-Kobayashi-Maskawa matrix element, G_F the Fermi weak coupling constant, and

$$\lambda(q^2) = (m_B^2 + m_\pi^2 - q^2)^2 - 4m_B^2 m_\pi^2. \tag{4}$$

The decay rate vanishes at $q^2 = q^2_{\rm max}$, where the lattice simulation is most reliable. For the larger momentum transfer the lattice calculation suffer from the larger systematic error

of $O((ap)^2)$. In order to determine $|V_{ub}|$ model independently, therefore, it is essential to calculate $f^+(q^2)$ in a q^2 region where the experimental data will become available and the systematic error does not spoil the reliability of a simulation.

Recently CLEO Collaboration reported the first measurement of this decay mode, which gave the branching fraction of this process $(1.8 \pm 0.4 \pm 0.3 \pm 0.2) \times 10^{-4}$ [5]. Though current statistics of the experimental data ($2.84 \times 10^6 B\bar{B}$ pairs) is not enough to determine $|V_{ub}|$ precisely, B Factories will provide enough statistics ($10^8 B\bar{B}$ pairs).

Heavy quark effective theory Heavy quark effective theory (HQET) has much advanced our understanding of the heavy-light systems [6]. Especially in the case of semileptonic decays $B \to D, D^*$, six form factors are expressed in terms of single universal function known as the Isgur-Wise function. In a system containing single heavy quark, the momentum transfer between the heavy quark and the light degrees of freedom are of order $\Lambda_{\rm QCD}$ and much less than M_Q, hence the velocity of the heavy quark is almost unchanged. In the limit of $m_Q \to \infty$, the dynamics does not depend on the flavor (mass) and spin of the heavy quark ('heavy quark symmetry'). HQET makes use of this fact to remove the large mass scale m_Q from the dynamics and to incorporate the $1/m_Q$ power correction. The nonrelativistic QCD, which we use in this work to describe the heavy quark, can realized as a special case of HQET with the vanishing heavy quark classical velocity.

In the case of $B \to \pi$ decay, HQET predicts that the properly normalized matrix element has a static limit, which depends only on the velocity of the heavy meson, $v_\mu = p_\mu/m_B$, and the mass and the momentum of the pion [7]:

$$\frac{\langle \pi(\boldsymbol{k})|V_\mu^\dagger|B(\boldsymbol{p})\rangle}{\sqrt{m_\pi m_B}} = \theta_1(v\cdot k)v_\mu + \theta_2(v\cdot k)\frac{k_\mu}{v\cdot k}. \tag{5}$$

The finite mass correction enters into this expression as the power series of the inverse heavy meson mass, $1/m_B$. Evaluation of this correction is one of main topics of this work.

heavy meson effective theory In HQET, the fundamental degree of freedom is that of the heavy quark. One can use, alternatively, the meson degrees of freedom such as B and B^*, in the same manner as in the chiral effective theory [8, 9, 10]. This heavy meson effective theory, together with the chiral effective theory for the light mesons, can give the form factors of various matrix elements with several phenomenological parameters. Applying it to the case of $B \to \pi$ leads [10]

$$f^\pm(q^2) = \frac{1}{2}\frac{f_B}{f_\pi}\left[1 - \frac{f_{B^*}}{f_B}\left\{\lambda\left(1+\frac{v\cdot k}{2m_b}\right) + (\lambda_1-\lambda_2)\frac{\Lambda}{m_b}\right\}\frac{2m_b(v\cdot k \mp m_B)}{q^2 - m_{B^*}^2}\right]. \tag{6}$$

where $v \cdot k = (m_B^2 + m_\pi^2 - q^2)/2m_B$, and m_b is the b-quark mass. λ, λ_1, λ_2, and Λ are phenomenological parameters to be fixed comparing with experiments. f^+ and f^- are defined as

$$\langle \pi(k)|V_\mu|B(p)\rangle = f^+(q^2)(p+k)_\mu - f^-(q^2)(p-k)_\mu. \tag{7}$$

Eq. (6) implies that near the zero recoil point, dominant contribution to $f^+(q^2)$ comes from the B^* pole. In Section 4.2, we discuss that to what extent this pole behavior is observed in our numerical result. It is generally believed that the heavy meson theory is applicable only in the region where the momentum transfer is order of $\Lambda_{\rm QCD}$, and not reliable in the hard scattering region.

Soft pion theorem In the chiral limit, in which the pion mass vanishes, the soft pion theorem relate f^0 at the zero recoil to the B meson decay constant, f_B [9, 10, 11]:

$$f^0(q^2_{\rm max}) = \frac{f_B}{f_\pi}, \tag{8}$$

where $f_\pi = 131\ MeV$ is the pion decay constant. This relation should be satisfied if the numerical simulations correctly reproduce the chiral limit. As mentioned below, we use the standard Wilson action to describe the light quark, which breaks chiral symmetry explicitly. Thus this relation plays an important role to examine proper incorporation of the chiral symmetry on the lattice. For the finite light quark mass case, with a help of the heavy meson effective theory, the relation between $f^0(q^2_{\rm max})$ and f_B becomes [10]

$$f^0(q^2_{\rm max}) = \frac{m_B}{m_B + m_\pi}\frac{f_B}{f_\pi}. \tag{9}$$

This expression is helpful to argue the chiral extrapolation of the results obtained at finite light quark masses.

1.3 The Lattice Simulations for the semileptonic decay form factors; status and the present work

Here we briefly survey lattice works of semileptonic form factors which have been done and are now under investigation and then state our simulation condition in comparison with them. Several remarks on the notation used in this thesis is also given.

Status of lattice works Here we summarize the current status of works on the semileptonic $B \to (light\ meson)$ decays. Calculations of these processes, such as $B \to \pi$, ρ, K^*, can be treated in almost same manner, while photodecay $b \to s\gamma$ channels requires the values at $q^2 = 0$ for physical applications. Table 1 summarize the works

performed previously and now under going. Until now all calculations are in the quenched approximation, in which virtual quark polarization effect is not included.

The early works include an extrapolation from the charm mass region to the b-quark mass scale. ELC [15], APE [16], and UKQCD [19, 20, 21] Collaborations make use of the HQET prediction, Eq. 5, to assume the extrapolation form. On the other hand, Wuppertal group [22] first fit their results to several pole-type functions in the charm region, then extrapolate $f(q^2 = 0)$ to the B meson mass with several functional form. These extrapolation inevitably cause systematic uncertainties, thus the direct simulation at b-quark mass is essentially important to get reliable answer.

To carry out direct simulations at b-quark with currently available computer power, certain effective theory is called for. In this work, we describe the heavy quark using NRQCD up to $O(1/m_Q)$. NRQCD has been applied to the heavy-heavy systems [28] and the heavy-light systems [14, 29], and obtained successful results.

An alternative approach is use of the clover action with realization as an effective theory, *i.e.* the Fermilab action [35]. This procedure is employed by FNAL [12] and JLQCD [23] collaborations. Fermilab action is realized as the expansion of QCD in the quark's momentum, and its leading order and next-to-leading order expressions correspond to the Wilson and the clover actions respectively. An advantage of the Fermilab action is applicability to an arbitrary mass values, so that it is convenient for the calculations around c-quark mass. On the other hand, further improvement beyond the clover action is much more difficult than in NRQCD, where $O(1/m_Q^2)$ correction is easily incorporated. Of course the results from these approaches should be consistent if the lattice simulations reliably reproduce the continuum physics.

The effective theory approaches are no longer necessary when sufficiently large computer is available to deal with a lattice cutoff much larger than m_b. However, even if such calculations are possible for quenched lattice, present lattice algorithms to simulate dynamical quarks require further enormous computer power for such a lattice as large as we could not reach in forthcoming decade. Therefore the use of effective theories is essential to make use of the lattice results, at least with dynamical quarks, for the analysis with experimental data from the B Factories. In addition, the effective theory approaches enable us to carry out efficient calculations on rather small computers.

Summary of the lattice setup Now we turn to the summary of our lattice setup in the present investigation. We calculate the matrix elements of $B \to \pi$ process using the heavy quark described by NRQCD up to $O(1/m_Q)$ terms and the Wilson light quark. The simulation is carries out on a lattice of size $16^3 \times 32$ at $\beta = 5.8$, in the quenched approximation. The lattice cutoff at this β is $a^{-1} = 1.7\ GeV$, which is obtained using ρ

Group	β	Actions (heavy-light)	m_Q	m_q	Refs.
ELC	6.4	Wilson-Wilson	$\sim m_c$	chiral limit	[15]
APE	6.0	clover-clover	$\sim m_c$	chiral limit	[16, 17]
LANL	6.0	Wilson-Wilson	$\sim m_c$	chiral limit	[18]
UKQCD	6.2	clover-clover	$\sim m_c$	$\sim m_s$	[19, 20, 21]
Wuppertal	6.3	Wilson-Wilson	$\sim m_c$	chiral limit	[22]
FNAL	5.9	clover-clover	m_c, m_b, ∞	$\sim m_s$	[12]
Hiroshima	5.8	NRQCD-Wilson	m_c–m_b	chiral limit	this work
JLQCD	5.9	clover-clover	m_c–m_b	chiral limit	[23]

Table 1: Current works on semileptonic decays of $B \to (\textit{light meson})$. The results from JLQCD Collaboration is preliminary.

meson mass. This lattice spacing is somewhat coarse compared with currently available lattices, but convenient for an exploratory study at various masses and various momenta. Instead the ρ meson mass, a^{-1} from the string tension amounts $a^{-1} \sim 1.4\ GeV$, which shows an scale ambiguity caused by the use of quenched approximation and the use of rather coarse lattice.

We investigate the heavy quark mass dependence of the form factors, by taking the mass of the heavy quark to cover a range of 1.5–8 GeV. In the range around the charm quark mass, $O(1/m_Q^2)$ correction would be large. The use of the Wilson light quark leads a $O(a\Lambda_{\rm QCD})$ uncertainty, which is one of most significant systematic error of this simulation. In future calculation, the clover action is called for to reduce this effect to $O(a^2\Lambda_{\rm QCD}^2)$.F To investigate the whole feature of the form factors, we measure more values of initial and final state momenta than previous works, which amount 20 points of q^2.

To obtain the physical values of the matrix elements, we need two additional procedures, the renormalization correction and the chiral extrapolation. The former is perturbatively evaluated in Section 2.3. For reasons mentioned in Section 2.3, this is only for a estimation of the size of the correction. The chiral extrapolation is discussed at the end of Section 3. It is found that these two procedures are crucial to obtain the physics results. Besides these, there are several subtle problems, which should be clarified in future calculations.

Notations We denote the heavy-light and the light-light pseudoscalar mesons as B and π mesons, respectively, regardless of actual masses of their heavy and light quarks for simplicity. The momenta of B meson and pion is always expressed by the symbols $\boldsymbol{p}$ and $\boldsymbol{k}$ respectively.

Without specifying, from now on we describe the all quantities in the lattice unit. For example, the number '2.6' in the expression '$m_Q = 2.6$' is in the lattice unit and a^{-1} must be multiplied to express in the physical unit. When we denote them in the physical unit, the unit, *e.g.* 'GeV', is used explicitly. To convert lattice results into the physical unit, we use the inverse lattice spacing $a^{-1} = 1.714(63)\ GeV$ determined from the ρ meson mass on our lattice.

2 LATTICE FORMULATION

This section describes NRQCD formulation of the heavy quark, and how we evaluate the matrix element in the numerical simulation.

The lattice actions for the gauge field and the light quark field are most standard ones [34]. The gauge field action is

$$S_{\rm gauge} = \beta \sum_{x,\mu\nu} \left(1 - \frac{1}{3}{\rm ReTr}U_{\mu\nu}(x)\right), \tag{10}$$

where $U_{\mu\nu}(x) = U_\mu(x)U_\nu(x+\hat{\mu})U_\mu^\dagger(x+\hat{\nu})U_\nu^\dagger(x)$. The coupling parameter $\beta = 6/g^2$ adjusts the lattice spacing implicitly.

The light quark is described with the Wilson action:

$$S_{\rm light} = \beta \sum_{xy} \bar{q}(x)K(x,y)q(y), \tag{11}$$

$$K(x,y) = \delta_{xy} - \kappa \sum_\mu \left[(1-\gamma_\mu)U_\mu(x)\delta_{x+\hat{\mu},y} + (1+\gamma_\mu)U_\mu^\dagger(x-\hat{\mu})\delta_{x-\hat{\mu},y}\right], \tag{12}$$

where κ is the hoping parameter which controls the light quark mass. For the light quark field normalization, we adopt tadpole improved form $\sqrt{1-3\kappa/4\kappa_c}$ [37], where κ_c is the critical hopping parameter which corresponds to the vanishing quark mass limit.

Present calculation is performed in the quenched approximation, in which the dynamical quark effect is neglected. In this case, the expectation value of an operator $F[U]$ is expressed as

$$\langle F \rangle = \int \mathcal{D}U F[U] \exp(-S_{\rm gauge}). \tag{13}$$

In the simulation, this expectation values are evaluated on the configurations which are generated in the weight $\exp(-S_{\rm gauge})$.

2.1 Lattice NRQCD action

The lattice NRQCD [24] has been extensively used for the investigations of the heavy-heavy systems [28] and hadrons containing a single heavy quark [14, 29]. It is designed to remove the large mass scale m_Q from the theory using the $1/m_Q$ expansion and to reproduce the same results as of the relativistic QCD up to a given order of $1/m_Q$. The NRQCD action is derived by applying the Foldy-Wouthuysen-Tani transformation to the Dirac spinor field. One of the best advantages of the NRQCD is that the $1/m_Q$ corrections can be easily incorporated. In fact, NRQCD including the $O(1/m_Q^2)$ corrections has been applied to the spectroscopy and the decay constant of the heavy-light system, as well as to those of the quarkonium system.

In this work, we employ the lattice NRQCD action including the $O(1/m_Q)$ terms[1]

$$S_{\rm NRQCD} = \sum_x Q^\dagger(x) \left[\left(1 - \frac{1}{2n} H_0\right)^{-n} U_4 \left(1 - \frac{1}{2n} H_0\right)^{-n} Q(x+\hat{4}) - (1-\delta H) Q(x) \right], \tag{14}$$

where

$$H_0 = -\frac{1}{2m_Q}\Delta^{(2)}, \tag{15}$$

$$\delta H = -\frac{1}{2m_Q}\boldsymbol{\sigma}\cdot\boldsymbol{B}, \tag{16}$$

and $Q(x)$ is the effective two component spinor field, which describes the heavy quark. $\Delta^{(2)}$ denotes the three dimensional Laplacian,

$$\Delta^{(2)} Q(x) = \sum_i \left[U_i(x) Q(x+\hat{i}) + U_i^\dagger(x-\hat{i}) Q(x-\hat{i}) - 2Q(x) \right]. \tag{17}$$

$\boldsymbol{\sigma}$ is the Pauli matrices, and $\boldsymbol{B}$ is the standard clover-leaf type chromomagnetic field, $B_i = \epsilon_{ijk} F_{jk}/2$, with

$$F_{\mu\nu} = -\frac{1}{4} \sum_{P(x,\mu\nu)} I(U_{P(x,\mu\nu)}), \tag{18}$$

where $P(x,\mu\nu)$ means four plaquette which open at the site x and lie in (μ,ν) plane. The operator $I(M)$ make a matrix $(-iM)$ hermitian and traceless:

$$I(M) = \frac{M - M^\dagger}{2i} - \frac{1}{3}{\rm Im}[{\rm Tr} M]. \tag{19}$$

This action generates the following evolution equation

$$G_Q(\boldsymbol{x}, t=1) = \left(1 - \frac{1}{2n} H_0\right)^n U_4^\dagger \left(1 - \frac{1}{2n} H_0\right)^n G_Q(\boldsymbol{x}, t=0), \tag{20}$$

$$G_Q(\boldsymbol{x}, t+1) = \left(1 - \frac{1}{2n} H_0\right)^n U_4^\dagger \left(1 - \frac{1}{2n} H_0\right)^n (1-\delta H)\, G_Q(\boldsymbol{x}, t). \tag{21}$$

To avoid the singular behavior of high frequency modes in the evolution equation, the stabilizing parameter n is chosen to satisfy the condition $|1 - H_0/2n| < 1$, which leads to $n > 3/2m_Q$. From a viewpoint of the perturbation theory, further constraint, $H_0/2n < 1$, is necessary to avoid singularities in some of vertices derived from the action (14). This point is again discussed in the last part of this section in connection with our choice of n in the simulation and the perturbative calculation.

[1] This action differ from that we used in our previous study of f_B [30], which is organized to remove $O(a\Lambda_{QCD}/m_Q)$ error, at the cost of simulation speed.

We apply the tadpole improvement procedure to this evolution equation according to [36],

$$U_\mu(x) \to U_\mu(x)/u_0, \tag{22}$$

where u_0 is plaquette-defined mean field value of link variable, $u_0 = \langle \mathrm{Tr} U_{\mathrm{plaq}}/3 \rangle^{1/4}$.

The four component spinor field $\psi(x)$ of the heavy quark is expressed in terms of two component spinor field $Q(x)$ as

$$\psi(x) = \left(1 - \frac{\boldsymbol{\gamma}\cdot\boldsymbol{\Delta}}{2m_Q}\right)\begin{pmatrix} Q(x) \\ 0 \end{pmatrix}, \tag{23}$$

where $\boldsymbol{\Delta}$ is the symmetric lattice covariant derivative,

$$\Delta_i Q(x) = U_i(x)Q(x+\hat{i}) - U_i^\dagger(x-\hat{i})Q(x-\hat{i}). \tag{24}$$

$O(1/m_Q)$ correction appears in the lower component of $\psi(x)$, which affects the heavy-light current.

2.2 Correlation functions

We employ the standard simulation technique to calculate the hadronic matrix elements of the semileptonic decay. We calculate the three-point correlation functions

$$C_\mu^{(3)}(\boldsymbol{p},\boldsymbol{k};t_f,t_s,t_i) = \sum_{\boldsymbol{x}_f}\sum_{\boldsymbol{x}_s} e^{-i\boldsymbol{p}\cdot\boldsymbol{x}_f} e^{-i(\boldsymbol{k}-\boldsymbol{p})\cdot\boldsymbol{x}} \ \langle 0|O_B(\boldsymbol{x}_f,t_f)V_\mu^\dagger(\boldsymbol{x}_s,t_s)O_\pi^\dagger(\boldsymbol{0},t_i)|0\rangle, \tag{25}$$

where O_B and O_π are the interpolating operators for B and π mesons, respectively, and $V_\mu = \bar{q}\gamma_\mu\psi$ is the heavy-light vector current. Figure 2 shows our setup of the source, the current, and the sink operators.

As mentions in Section 1.3, we denote the heavy-light and the light-light pseudoscalar mesons as B and π, respectively, regardless of their mass parameters κ and m_Q for simplicity. For $t_f \gg t_s \gg t_i$ the correlation function Eq. (25) becomes

$$C_\mu^{(3)}(\boldsymbol{p},\boldsymbol{k};t_f,t_s,t_i) \to \frac{Z_B(\boldsymbol{p})}{2E_B(\boldsymbol{p})}\frac{Z_\pi(\boldsymbol{k})}{2E_\pi(\boldsymbol{k})} e^{-E_{\bar{q}Q}(\boldsymbol{p})(t_f-t_s)} e^{-E_\pi(\boldsymbol{k})(t_s-t_i)} \langle B(\boldsymbol{p})|V_\mu^\dagger|\pi(\boldsymbol{k})\rangle_{\mathrm{latt}}, \tag{26}$$

where $E_B(\boldsymbol{p})$ and $E_\pi(\boldsymbol{k})$ denote the energy of B meson and pion, respectively. The exponent $E_{\bar{q}Q}(\boldsymbol{p})$ is not the total energy but the binding energy of the B meson, because the heavy quark mass m_Q is subtracted in the NRQCD. We use the local interpolating operators for both of B and π,

$$O_B(x) = \bar{q}(x)\gamma_5 Q(x), \qquad O_\pi(x) = \bar{q}(x)\gamma_5 q(x), \tag{27}$$

and

$$Z_B(\boldsymbol{p}) = \langle 0|O_B(0)|B(\boldsymbol{p})\rangle, \qquad Z_\pi(\boldsymbol{k}) = \langle 0|O_\pi(0)|\pi(\boldsymbol{k})\rangle \tag{28}$$

are their matrix elements.

In calculating Eq. (25) we vary t_f with fixed t_i and t_s in order to find out the region where the correlation functions are dominated by the ground state. The fixed t_s is chosen so that the pion two-point correlation function is dominated by the ground state, as is shown in Section 3.

Using the quark propagators, Eq. (25) is expressed as

$$\begin{aligned} C_\mu^{(3)}(\boldsymbol{p},\boldsymbol{k};t_f,t_s,t_i) &= \sum_{\boldsymbol{x}_f}\sum_{\boldsymbol{x}_s} e^{-i\boldsymbol{p}\cdot\boldsymbol{x}_f} e^{-i(\boldsymbol{k}-\boldsymbol{p})\cdot\boldsymbol{x}} \\ &\quad \times \mathrm{Tr}\left[S_q^\dagger(x_f,x_i) S_Q(x_f,x_s)\left(1+\frac{\boldsymbol{\gamma}\cdot\boldsymbol{D}^\dagger}{2m_Q}\right)\gamma_\mu S_q(x_s,x_i)\right], \end{aligned} \tag{29}$$

where spinor and color indices are suppressed. S_q is the light quark propagator, which is obtained by solving the equation $K(y,x)S_q(x,x_i) = \delta_{x,x_i}$ with suitable iterative solver algorithm. The heavy quark propagator, S_Q, has 2×2 components in spinor space, hence relevant components of S_q are selected.

The computational steps are as follows: (i) determine the light quark propagator with the source $(\boldsymbol{0},t_i)$, (ii) at the time slice t_s, obtain $b(x)$ by multiplying the current matrix, heavy quark correction operator, and momentum transfer factor to the light quark propagator $S_q(x_s)$:

$$b(x_s) = e^{-i(\boldsymbol{k}-\boldsymbol{p})\cdot\boldsymbol{x}_s}\left(1+\frac{1}{2m_Q}\boldsymbol{\gamma}\cdot\boldsymbol{D}^\dagger\right)\gamma_\mu S_q(x_s,x_i), \tag{30}$$

(iii) then using $b(x_s)$ as the source, solve the heavy quark evolution equation, (iv) finally at the sink $(\boldsymbol{x}_f,t_f)$ combine the heavy with the light qaurk propagator and multiply $\exp(-i\boldsymbol{p}\cdot\boldsymbol{x}_f)$, and sum up.

To obtain $E_{\bar{q}Q}(\boldsymbol{p})$, $E_\pi(\boldsymbol{k})$, $Z_B(\boldsymbol{p})$ and $Z_\pi(\boldsymbol{k})$, we also calculate the two-point correlation functions with finite momenta

$$C_B^{(2)}(\boldsymbol{p};t_f,t_i) = \sum_{\boldsymbol{x}_f} e^{-i\boldsymbol{p}\cdot\boldsymbol{x}_f}\langle O_B(x_f)O_B^\dagger(x_i)\rangle \to \frac{Z_B(\boldsymbol{p})^2}{2E_B(\boldsymbol{p})}\exp(-E_{\bar{q}Q}(\boldsymbol{p})(t_f-t_i)), \tag{31}$$

$$C_\pi^{(2)}(\boldsymbol{k};t_f,t_i) = \sum_{\boldsymbol{x}_f} e^{-i\boldsymbol{k}\cdot\boldsymbol{x}_f}\langle O_\pi(x_f)O_\pi^\dagger(x_i)\rangle \to \frac{Z_\pi(\boldsymbol{k})^2}{2E_\pi(\boldsymbol{k})}\exp(-E_\pi(\boldsymbol{k})(t_f-t_i)). \tag{32}$$

Combining Eqs.(26), (31), and (32), one can easily see that the matrix element is expressed as

$$\langle B(\boldsymbol{p})|V_\mu^\dagger|\pi(\boldsymbol{k})\rangle_{\rm latt} = \sqrt{2E_B(\boldsymbol{p})}\sqrt{2E_\pi(\boldsymbol{k})}\frac{e^{E_{\bar{q}Q}(t_f-t_s)}}{\tilde{Z}_B(\boldsymbol{p})}\frac{\tilde{Z}_\pi(\boldsymbol{k})}{C_\pi^{(2)}(\boldsymbol{k};t_s,t_i)}C_\mu^{(3)}(\boldsymbol{p},\boldsymbol{k};t_f,t_s,t_i) \tag{33}$$

Figure 2: The three-point correlation function to obtain the matrix element.

for $t_f \gg t_s \gg t_i$, where $\tilde{Z} = Z/\sqrt{2E}$. As expressed in Eq. (33), we use the two-point correlation function itself to cancel the exponentially decaying factor of pion, while use the values of $E_{\bar{q}Q}$ obtained by fits to cancel the B meson's. One reason of this asymmetric procedure is that the pion two-point function is constructed from the light quark propagator with a point source at $t_i = 4$, which is what we used to calculate the three-point function (25), and then we expect the statistical fluctuation mostly cancels between (25) and (32), while for the B meson exponential function, such a cancellation is not expected. In addition, as we mention in the next section, the two-point correlation function of B meson with the point source (31) requires larger time separation to reach the plateau than the three-point function (25), for which the heavy quark source is effectively 'smeared' at t_s.

2.3 Perturbative corrections

Beyond the tree level, certain renormalization prescription is required to obtain a physical quantity from the result of lattice calculation. We evaluate the perturbative corrections to the current and the heavy quark mass, using the lattice perturbation theory at the one-loop level.

To relate the matrix element in the lattice theory to that in the continuum QCD, operator matching is required [26]. We have calculated the perturbative renormalization factor Z_{V_μ} for the vector current [31]

$$V_\mu^{\rm cont} = Z_{V_\mu}\, V_\mu^{\rm latt} = Z_{V_\mu}\, \bar{q}\gamma_\mu\psi, \tag{34}$$

$(m_Q\ ,\ n)$	A	B	C_{V_4}	C_{V_i}
$(5.0\ ,1)$	0.0759	0.0124(4)	0.0210(11)	−0.0790(10)
$(2.6\ ,2)$	0.0668	0.0353(3)	0.0004(9)	−0.0780(7)
$(2.1\ ,2)$	0.0623	0.0449(3)	−0.0068(9)	−0.0757(7)
$(1.5\ ,3)$	0.0528	0.0623(2)	−0.0192(8)	−0.0734(6)
$(1.2\ ,3)$	0.0446	0.0757(1)	−0.0283(8)	−0.0707(6)
$(0.9\ ,6)$	0.0309	0.0933(1)	−0.0428(8)	−0.0687(5)

Table 2: The tadpole improved one-loop coefficients for the perturbative corrections E_0, Z_m, Z_{V_4}, and Z_{V_i}. Quoted errors represent the numerical uncertainties in the evaluation of loop integrals. The uncertainty of A is less than 10^{-4}.

where q is the Wilson light quark and ψ is defined in Eq. (23). Z_V is the ratio of the on-shell S-matrix elements in the continuum theory with $\overline{\rm MS}$ scheme and that in the lattice theory. In our definition, Z_V contains the leading logarithmic term, $\alpha \log(m_Q a)$, which comes from the continuum renormalization factor.

In calculating Z_V we use the massless Wilson quark and the external momenta are taken to be zero. We did not take into account the one-loop operator mixing with higher derivative operators, since there are already $O(a)$ errors at tree-level from the Wilson quark action. The one-loop coefficient is modified with the tadpole improvement [36]. For the mean link variable we use $u_0 = \langle TrU_{\rm plaq}/3\rangle^{1/4}$ except for the light quark wave function renormalization, for which we use another possible definition, $u_0 = 1/8\kappa_c$ [37]. Their one-loop perturbative expressions are used to determine the perturbative coefficients of Z_{V_μ}.

The results for the one-loop coefficient C_{V_μ} in

$$Z_{V_\mu} = 1 + g^2 C_{V_\mu} \tag{35}$$

are presented in Table 2 for several values of (m_Q, n). These values contain the leading logarithmic contribution, $\log(m_Q a)/4\pi^2$. The values of Z_{V_μ} with two choices of the lattice coupling constant $g_V^2(\pi/a) = 2.19$ and $g_V^2(1/a) = 3.80$ are plotted as a function of $1/m_Q$ in Fig. 3. (These coupling values are explained at the end of this section.) We observe that the spatial component of the vector current receives larger perturbative corrections than the temporal one. On the other hand, the $1/m_Q$ dependence is rather stronger for Z_{V_4} than for Z_{V_i}.

When we discuss the $1/m_B$ dependence of the renormalized matrix elements in Sec-

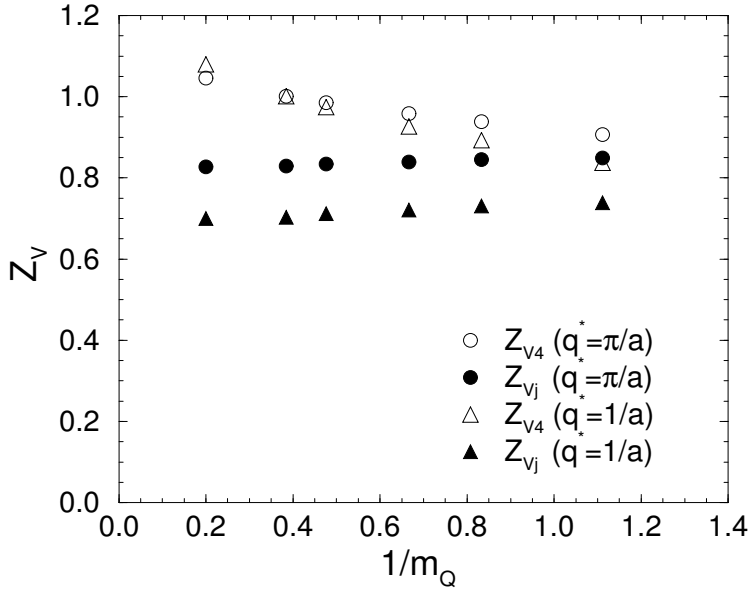

Figure 3: Renormalization constant for the vector current with two scales for the coupling constant, $q^\star = \pi/a$ and $1/a$. The open and filled symbols represent Z_{V_4} and Z_{V_j}, respectively.

tion 4, we multiply the leading logarithmic factor

$$\Theta(m_B/m_B^{(\mathrm{phys})}) = \left(\frac{\alpha_V(m_B)}{\alpha_V(m_B^{(\mathrm{phys})})}\right)^{2/11} \tag{36}$$

to cancel the logarithmic divergence in the infinite heavy quark mass limit due to the anomalous dimension of the heavy-light current.

The calculation of heavy quark self-energy leads to the energy shift E_0, heavy quark mass renormalization Z_m, and the heavy quark field renormalization [25]. The first two quantities appeared in the mass relation of heavy-light meson, and the last one is necessary to calculate Z_{V_μ}. B meson mass is given through the binding energy of the heavy-light meson, $E_{q\bar{Q}}(\boldsymbol{p}=0)$, as

$$m_B = Z_m m_Q - E_0 + E_{\bar{q}Q}(\boldsymbol{p}=0), \tag{37}$$

where E_0 and Z_m are obtained perturbatively

$$Z_m = 1 + g^2 B, \tag{38}$$

$$E_0 = g^2 A. \tag{39}$$

The tadpole improved coefficients A and B are also given in Table 2. These coefficients are determined by the numerical procedure proposed in [27].

For a historical reason, the stabilizing parameter we have used does not always satisfy the condition $n > 3/m_Q$, which is necessary to avoid divergent tree level vertices, while the simulation itself is stable with the condition $n > 3/2m_Q$. We, therefore, quote the results at tree level in the later sections as our main results. We estimate the size of the renormalization effect with the one-loop coefficients obtained with the combinations of m_Q and n, for which n's are larger than those we have used in the simulation and the perturbation theory exists. Although this estimation is certainly incorrect, it gives some idea for the one-loop effect, especially because the n-dependence of the simulation results is observed to be very small (Section 3.4).

The values of coupling constant are determined as follows. Lepage and Mackenzie [36] pointed out that when we use appropriately defined coupling constant, the lattice perturbatation theory works better than as it had been considered. According to them, we adopt one of such definitions, α_V, which is defined with the expectation value of the plaquette using its two-loop perturbative expression,

$$-\ln\langle \frac{1}{3}U_{\rm plaq} \rangle = \frac{4\pi}{3}\alpha_V(3.41/a)[1 - 1.19\alpha_V]. \tag{40}$$

In this work, we evaluate the perturbative corrections at two scales, π/a and $1/a$, to which α_V is made run using the two-loop β function. Using our numerical value, $\langle U_{\rm plaq}/3\rangle = 0.567633(35)$, we obtain $\alpha_V(\pi/a) = 0.1742$, and $\alpha_V(1/a) = 0.3026$, which give above values of g_V^2.

3 SIMULATION DETAILS

In this section, we describe the numerical simulation in detail apart from discussions on physical implications of the results, which will be discussed in the next section. After summarizing the simulation parameters, two-point correlation functions of π and B mesons with finite momenta are discussed. We describe how to extract the matrix elements and the form factors from the three-point correlation functions. Finally, the chiral extrapolation of the matrix element is discussed.

3.1 Simulation parameters

The numerical simulations are performed on a $16^3 \times 32$ lattice with 120 quenched gauge configurations generated with the standard plaquette gauge action at β=5.8. Each configuration is separated by 2000 pseudo-heat-bath sweeps [38] after 20000 sweeps for thermalization and fixed to the Coulomb gauge [39]. The Wilson quark action is used for the light quark at three κ values 0.1570, 0.1585 and 0.1600, which roughly lie in the range $[m_s, 2m_s]$, and the critical hopping parameter is κ_c=0.16346(7). The boundary condition for the light quark is periodic and Dirichlet for spatial and temporal directions, respectively. We obtain the light quark propagator using the BiCGStab algorithm [40] with the Incomplete LU decomposition preconditioning [41]. The light quark field is normalized with the tadpole improved form $\sqrt{1-3\kappa/4\kappa_c}$ according to [37]. The tadpole improvement is also applied for both the NRQCD action and the current operator with the replacement of $U_\mu \rightarrow U_\mu/u_0$ using the average value of a single plaquette $u_0 = \langle \mathrm{Tr} U_{\mathrm{plaq}}/3 \rangle^{1/4} = 0.867994(13)$.

The lattice scale is determined from the ρ meson mass as a^{-1}=1.71(6) GeV, although we expect a large $O(a)$ error for m_ρ with the unimproved Wilson fermion. The results for the π and the ρ meson masses and the pion decay constant are summarized in Table 3.

The heavy quark mass m_Q and the stabilizing parameter n used in our simulation

	$\kappa = 0.1570$	0.1585	0.1600	κ_c
m_π	0.5677(30)	0.4933(33)	0.4118(37)	-
m_ρ	0.6747(54)	0.6214(72)	0.567(11)	0.448 (17)
f_π	0.1496(46)	0.1380(49)	0.1270(53)	0.1019(64)

Table 3: The values of m_π, m_ρ, and pion decay constant without renormalization. Fitting range is $t = 14 - 24$.

are

$$\begin{pmatrix} m_Q \\ n \end{pmatrix} = \begin{pmatrix} 5.0 \\ 1 \end{pmatrix}, \begin{pmatrix} 2.6 \\ 1 \end{pmatrix}, \begin{pmatrix} 2.1 \\ 1 \end{pmatrix}, \begin{pmatrix} 2.1 \\ 2 \end{pmatrix}, \begin{pmatrix} 1.5 \\ 2 \end{pmatrix}, \begin{pmatrix} 1.2 \\ 2 \end{pmatrix}, \begin{pmatrix} 1.2 \\ 3 \end{pmatrix}, \begin{pmatrix} 0.9 \\ 2 \end{pmatrix}, \tag{41}$$

where $m_Q = 2.6$ and 0.9 roughly correspond to b- and c-quark masses, respectively.

For m_Q=2.1 and 1.2 we performed two sets of simulations with different values of n, though the statistics is lower (=60) for $(m_Q, n) = (2.1, 2)$ and $(1.2, 3)$. Since the different choice of n introduces the different higher order terms in a in the evolution equation, the choice of n should not affect the physical results for sufficiently small a. The small dependence of the numerical results on n is also crucial for our estimation of the perturbative corrections.

The spatial momentum of the B meson ($\boldsymbol{p}$) and the pion ($\boldsymbol{k}$) is taken up to $|\boldsymbol{p}|$, $|\boldsymbol{k}| \leq \sqrt{3} \cdot 2\pi/16$, which corresponds to the maximum momentum of ~ 1.2 GeV in the physical unit. We measure the three-point correlation function at 20 different momentum configurations $(\boldsymbol{p}, \boldsymbol{k})$ as listed in Table 4. The momentum configurations which are equivalent under the lattice rotational symmetry are averaged, and the number of such equivalent sets are also shown in Table 4.

The light quark propagator is solved with a local source at t_i=4, which is commonly used for the two-point and three-point functions. The heavy-light vector current is placed at $t_s = 14$, which is chosen so that the pion correlation function is dominated by the ground state signal. The position of the B meson interpolating operator is varied in a range $t_f = 23 - 28$, where we observe a good plateau as shown later.

3.2 Light-light meson

In order to obtain the form factors reliably, it is crucial to extract the ground state of the B meson and the pion involving finite momentum properly. In Fig. 4 we show the effective mass plot of pions with finite momentum at $\kappa = 0.1570$ and 0.1600. The spatial momentum $\boldsymbol{k} = (k_x, k_y, k_z)$ is understood with the unit of $2\pi/16$. This notation will be used throughout this paper. Although higher momentum states are rather noisy, we can observe a plateau beyond $t = 14$. We fit the data with the single exponential function to obtain the energy $E_\pi(\boldsymbol{k})$ shown by the horizontal solid lines in Fig. 4.

Figure 5 shows the energy momentum dispersion relation of pion, where the solid lines represent the relation in the continuum $E_\pi(\boldsymbol{k})^2 = m_\pi^2 + \boldsymbol{k}^2$. We observe a small discrepancy between the above relation and the data, which indicates the discretization error. However the disagreement is about 1–1.5 standard deviation and only a few percent.

i_q	$\boldsymbol{p}^2$	$\boldsymbol{k}^2$	$\boldsymbol{q}^2$	$\boldsymbol{p}$	$\boldsymbol{k}$	$-\boldsymbol{q} = \boldsymbol{k} - \boldsymbol{p}$	$\sharp\,(\boldsymbol{p}, \boldsymbol{k})$
1	0	0	0	(0, 0, 0)	(0, 0, 0)	(0, 0, 0)	1
2		1	1		(0, 0, 1)	(0, 0, 1)	6
3		2	2		(0, 1, 1)	(0, 1, 1)	12
4		3	3		(1, 1, 1)	(1, 1, 1)	8
5	1	0	1	(0, 0, 1)	(0, 0, 0)	(0, 0, −1)	6
6		1($\perp$)	2	(0, 1, 0)	(0, 0, 1)	(0, −1, 1)	24
7		1($\uparrow\uparrow$)	0	(0, 0, 1)	(0, 0, 1)	(0, 0, 0)	6
8		1($\uparrow\downarrow$)	4	(0, 0, −1)	(0, 0, 1)	(0, 0, 2)	2
9		2($\perp$)	3	(1, 0, 0)	(0, 1, 1)	(−1, 1, 1)	24
10		2	1	(0, 0, 1)	(0, 1, 1)	(0, 1, 0)	24
11		3	2	(0, 0, 1)	(1, 1, 1)	(1, 1, 0)	24
12		3	6	(0, 0, −1)	(1, 1, 1)	(1, 1, 2)	8
13	2	0	2	(0, 1, 1)	(0, 0, 0)	(0, −1, −1)	12
14		1($\perp$)	3	(1, 1, 0)	(0, 0, 1)	(−1, −1, 1)	24
15		1	1	(0, 1, 1)	(0, 0, 1)	(0, −1, 0)	24
16		2($\perp$)	4	(0, 1, −1)	(0, 1, 1)	(0, 0, 2)	4
17		2($\uparrow\uparrow$)	0	(0, 1, 1)	(0, 1, 1)	(0, 0, 0)	12
18		2	2	(1, 1, 0)	(0, 1, 1)	(−1, 0, 1)	48
19		2	6	(1, −1, 0)	(0, 1, 1)	(−1, 2, 1)	16
20	3	0	3	(1, 1, 1)	(0, 0, 0)	(−1, −1, −1)	8

Table 4: The momentum combinations $(\boldsymbol{p}, \boldsymbol{k})$ used in the simulation. In this table, the values of $\boldsymbol{p}$, $\boldsymbol{k}$, and $\boldsymbol{q}$ are expressed in the unit of $2\pi/16$. The set which is equivalent with another under the lattice rotational symmetry is identified with the same i_q-number, and a representative is shown in the fifth through seventh columns. The last column shows the numbers of equivalent combinations. The symbols in the third column denote the direction of $\boldsymbol{k}$ against $\boldsymbol{p}$ as follows: $\perp$: orthogonal, $\uparrow\uparrow$: parallel, $\uparrow\downarrow$: anti-parallel, and oblique for others. The set $i_q = 12$ gives the minimum q^2 value among the sets in this table.

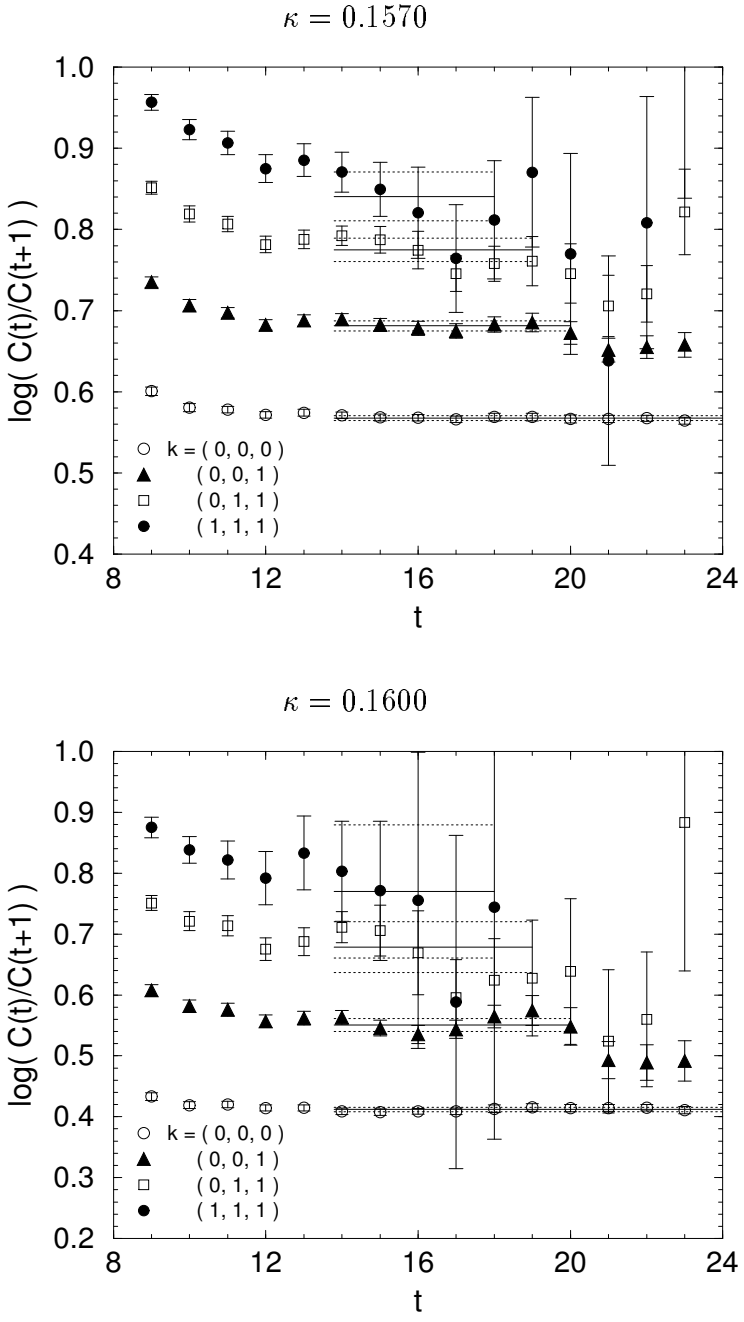

Figure 4: Effective mass plot of pion at $\kappa = 0.1570$ and 0.1600. The horizontal solid lines represent the fitted values and the fitting range with the statistical errors (dotted lines).

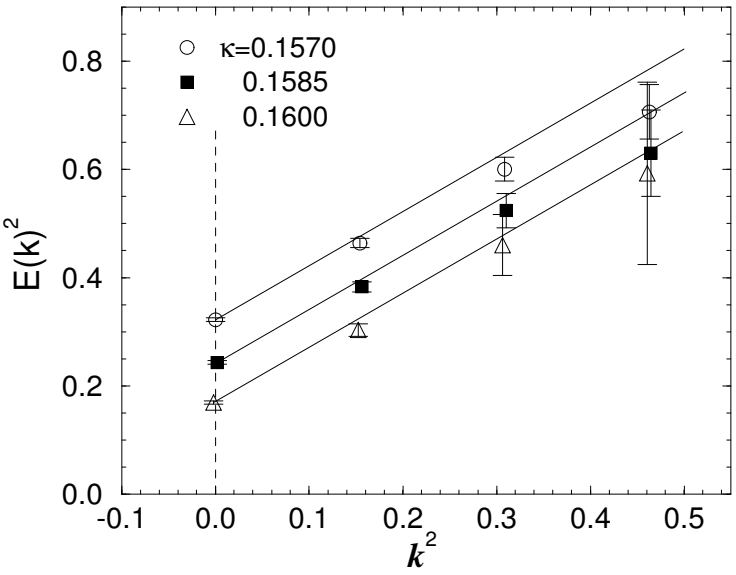

Figure 5: Dispersion relation for pion. The solid lines represent the relation $E_\pi^2(\boldsymbol{k}) = m_\pi^2 + \boldsymbol{k}^2$ with m_π the rest mass obtained in the simulation. For $\kappa = 0.1585$ and 0.1600, symbols are slightly shifted in horizontal direction for clarity.

3.3 Heavy-light meson

To compute the B meson two-point correlation functions, we employ the smeared source for heavy quark as well as the local source, with the local sink for both cases. The smearing function for the heavy quark is obtained with a prior measurement of the wave function with the local source. In Fig. 6 we plot the effective mass for both the local-local and the smeared-local correlation functions at $m_Q = 2.6$ and $\kappa = 0.1570$, 0.1600. The plateau is reached beyond $t = 16$ for the local-local, while the smeared-local exhibits clear plateau from even earlier time slices.

We obtain the binding energy with a fit range [16, 24] for both types of the correlation functions and for all momenta, and the results are consistent in all cases. The binding energy averaged over the results fitted from the local and the smeared sources are listed in Table 5 together with the values in the chiral limit. In Table 5, we also listed the binding energy for the vector meson B^* measured with the local-local correlation function, which are used in later discussions on the B^* pole contribution to the form factors. It is also worth to note that the values of $E_{\bar{q}Q}$ obtained with different stabilizing parameter n is consistent with each other within their statistical errors.

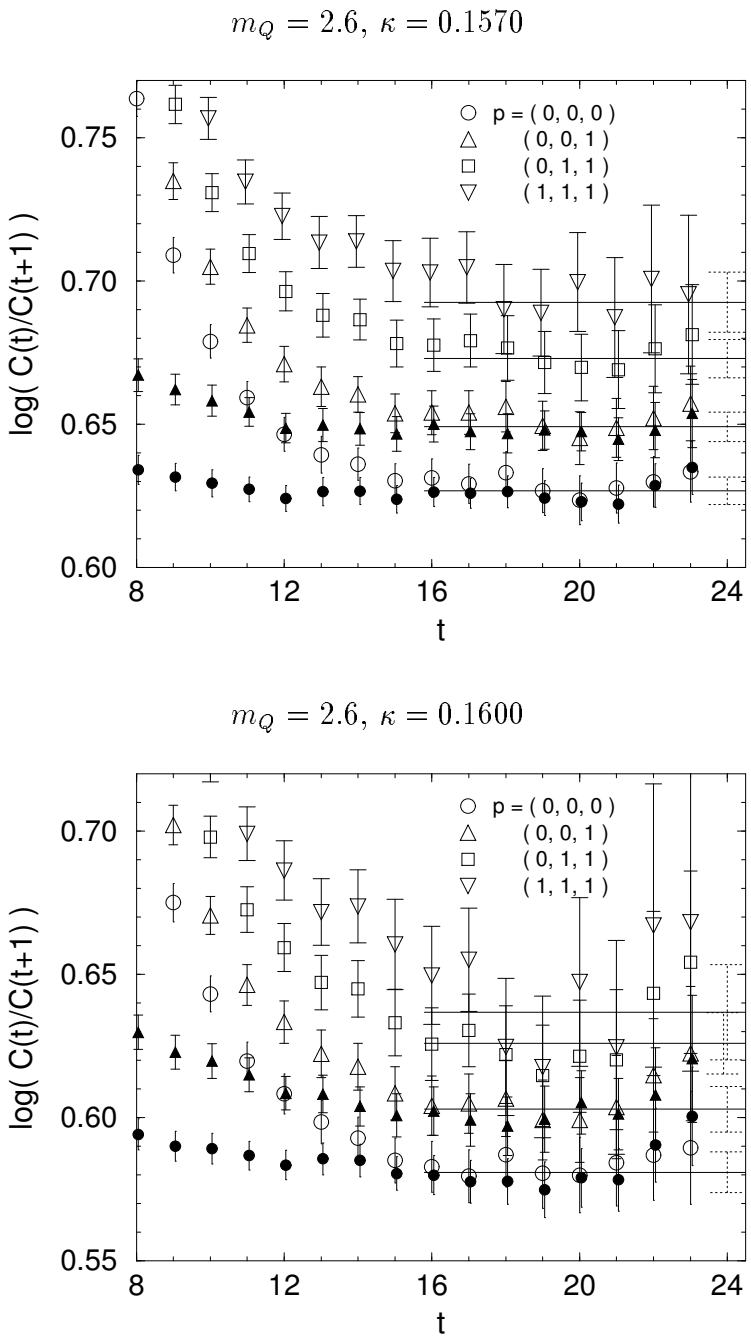

Figure 6: Effective mass plot of B meson at $m_Q = 2.6$ and $\kappa = 0.1570, 0.1600$. Results with the smeared source (filled symbols) are shown for $|\boldsymbol{p}|^2 = 0, 1$ as well as the results with the local source (open symbols). The horizontal solid lines express the average values over the results of single exponential fit of the local-local and the smeared-local correlation functions. The statistical errors of the fitted values are displayed at the right end of the lines. For all m_Q, κ, and momentum, the fit ranges are set to $t = 16 - 24$.

Pseudoscalar meson binding energy: $E_{\bar{q}Q}(\boldsymbol{p}=0)$

$(m_Q\ ,\ n)$	$\kappa = 0.1570$	0.1585	0.1600	κ_c
(5.0 , 1)	0.6304(69)	0.6084(83)	0.585 (11)	0.535 (15)
(2.6 , 1)	0.6268(48)	0.6041(56)	0.5809(71)	0.530 (10)
(2.1 , 1)	0.6247(45)	0.6014(52)	0.5777(65)	0.5260(91)
(2.1 , 2)	0.6279(53)	0.6056(62)	0.5834(80)	0.534 (11)
(1.5 , 2)	0.6180(42)	0.5940(48)	0.5696(59)	0.5162(81)
(1.2 , 2)	0.6135(40)	0.5889(46)	0.5640(56)	0.5095(75)
(1.2 , 3)	0.6142(51)	0.5899(56)	0.5655(68)	0.5117(92)
(0.9 , 2)	0.6058(39)	0.5805(43)	0.5551(51)	0.4991(68)

Vector meson binding energy: $E_{\bar{q}Q^*}(\boldsymbol{p}=0)$

$(m_Q\ ,\ n)$	$\kappa = 0.1570$	0.1585	0.1600	κ_c
(5.0 , 1)	0.649 (12)	0.628 (14)	0.604 (19)	0.555 (27)
(2.6 , 1)	0.6502 (62)	0.6287 (76)	0.6065 (99)	0.559 (14)
(2.1 , 1)	0.6501 (56)	0.6279 (68)	0.6047 (88)	0.555 (13)
(1.5 , 2)	0.6488 (52)	0.6257 (61)	0.6014 (79)	0.550 (11)
(1.2 , 2)	0.6484 (51)	0.6249 (59)	0.6002 (76)	0.547 (11)
(0.9 , 2)	0.6470 (50)	0.6231 (57)	0.5982 (73)	0.545 (10)

Table 5: The binding energy of the pseudoscalar and vector heavy-light mesons. The single exponential fit is applied with the fitting range $t = 16 - 24$. For the pseudoscalar we average the values obtained from the local-local and the smeared-local correlation functions. For the vector mesons we use the local-local only, and there is no data available for $(m_Q, n) = (2.1, 2)$ and $(1.2, 3)$.

The dispersion relation for the B meson takes the following nonrelativistic form

$$E_{\bar{q}Q}(\boldsymbol{p}) = E_{\bar{q}Q}(0) + \frac{1}{2m_{\rm kin}}\boldsymbol{p}^2 + O(1/m_B^3), \tag{42}$$

where the kinetic mass $m_{\rm kin}$ should agree with the rest mass m_B (37) in the continuum limit. Since we use the NRQCD action correct up to $O(1/m_Q)$, including higher order terms in $1/m_B$ in Eq. (42) does not make sense. In Fig. 7 $E_{\bar{q}Q}(\boldsymbol{p})$ is shown as a function of $\boldsymbol{p}^2$ at $m_Q = 2.6$. The solid lines represent the relation (42) with $m_{\rm kin} = m_B$ determined through the tree level relation $m_B = m_Q + E_{\bar{q}Q}(0)$, which reproduce the data quite well. With the one-loop correction (37) the agreement becomes even better as presented with the dashed lines in the figure.

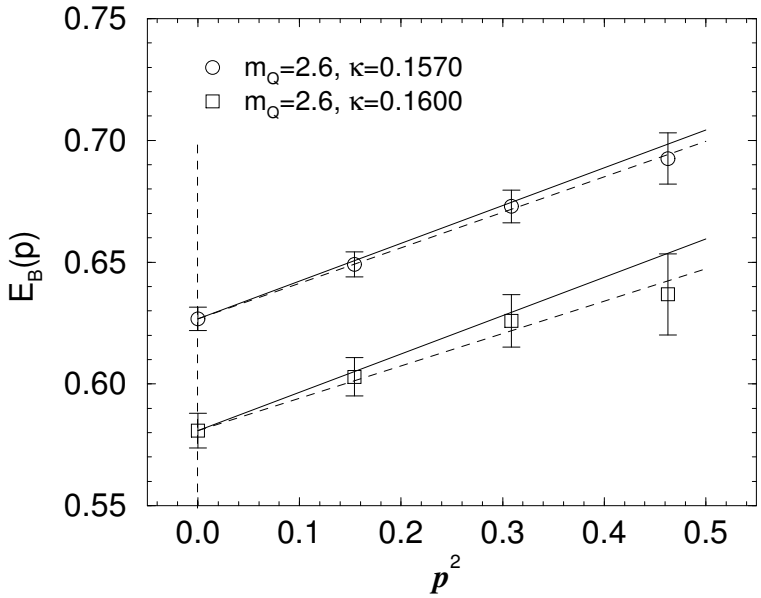

Figure 7: Dispersion relation for the B meson at $m_Q = 2.6$ and $\kappa = 0.1570$, 0.1600. The solid lines represent the relation $E_{\bar{q}Q}(\boldsymbol{p}) = E_{\bar{q}Q}(0) + \boldsymbol{p}^2/2m_B$, for which m_B is determined with the tree level formula $m_B = m_Q + E_{\bar{q}Q}(0)$. Dashed lines represent the same relation with the renormalized m_B at the scale $q^\star = 1/a$.

3.4 Three-point function and matrix elements

Figure 8 is the effective mass plot of the three-point function at $m_Q = 2.6$ and $\kappa = 0.1570$, 0.1600. The horizontal axis represents the time slice on which the B meson interpolating operator is put, and the vertical axis corresponds to the binding energy of the B meson. The horizontal solid lines represent the binding energy $E_{\bar{q}Q}(\boldsymbol{p})$ determined from the two-point correlation functions. The figures display that the three-point correlation functions are dominated by the ground states beyond $t = 23$, and there they give the consistent values for $E_{\bar{q}Q}(\boldsymbol{p})$ with ones extracted from the two-point functions. Therefore, in this region we can use Eq. (33) together with the results of the two-point correlation functions to extract the matrix elements.

It is useful to define the quantity $\hat{V}_\mu$ as

$$\hat{V}_\mu(\boldsymbol{p}, \boldsymbol{k}) = \frac{\langle B(\boldsymbol{p})|V_\mu^\dagger|\pi(\boldsymbol{k})\rangle_{\rm latt}}{\sqrt{2E_B(\boldsymbol{p})}\sqrt{2E_\pi(\boldsymbol{k})}}, \tag{43}$$

because it is defined only through the residue of the two- and three-point correlation functions without the knowledge how one defines the meson energies. Since there are uncertainties in the light-light and heavy-light meson dispersion relations, it is better to

i_q	q^2	$\hat{V}_4$	$\hat{U}_p$	$\hat{U}_k$
1	7.071 (20)	1.014 (34)	-	-
2	6.280 (19)	0.844 (26)	-	0.878 (41)
3	5.609 (19)	0.754 (50)	-	0.695 (61)
4	5.017 (18)	0.612 (87)	-	0.57 (10)
5	7.044 (20)	0.999 (36)	0.0475(28)	-
6	6.247 (19)	0.832 (28)	0.0366(47)	0.860 (41)
7	6.555 (19)	0.930 (30)	1.009 (46)	1.009 (46)
8	5.938 (19)	0.750 (34)	−0.702 (48)	0.702 (48)
9	5.571 (19)	0.742 (49)	0.040 (12)	0.674 (59)
10	5.880 (19)	0.827 (55)	0.790 (68)	0.767 (66)
11	5.283 (18)	0.66 (10)	0.65 (12)	0.63 (11)
12	4.666 (18)	0.544 (68)	−0.39 (12)	0.477 (82)
13	7.017 (20)	0.992 (42)	0.0467(30)	-
14	6.214 (19)	0.825 (34)	0.0360(48)	0.848 (45)
15	6.523 (19)	0.923 (38)	0.517 (26)	0.997 (51)
16	5.534 (19)	0.757 (76)	0.052 (53)	0.670 (82)
17	6.151 (19)	0.920 (67)	0.863 (77)	0.863 (77)
18	5.842 (19)	0.820 (58)	0.412 (36)	0.758 (68)
19	5.225 (19)	0.669 (52)	−0.266 (41)	0.587 (61)
20	6.990 (20)	0.968 (58)	0.0454 (33)	-

Table 6: $\hat{V}_4$, $\hat{U}_p$, and $\hat{U}_k$ in the lattice unit at $m_Q = 2.6$ and $\kappa = 0.1570$. i_q denotes the set of momentum $(\boldsymbol{p}, \boldsymbol{k})$ summarized in Table 4. In the evaluation of q^2, the B meson mass is determined through the tree level relation $m_B = m_Q + E_{\bar{q}Q}(0)$.

deal with the quantity which is free from the ambiguity. Moreover, $\hat{V}_\mu$ is the quantity which has the infinite mass limit in the heavy quark effective theory. When the perturbative correction is incorporated, $\Theta(m_B/m_B^{(\mathrm{phys})})$ given by Eq. (36) is multiplied to $\hat{V}_\mu$. Therefore $\hat{V}_\mu$ is suitable quantity to study the $1/m_Q$ dependence.

For the spatial components of $\hat{V}_\mu$, we also define the scalar products

$$\hat{U}_p(\boldsymbol{p}, \boldsymbol{k}) = \frac{\boldsymbol{p} \cdot \hat{\boldsymbol{V}}(\boldsymbol{p}, \boldsymbol{k})}{\boldsymbol{p}^2}, \qquad \hat{U}_k(\boldsymbol{p}, \boldsymbol{k}) = \frac{\boldsymbol{k} \cdot \hat{\boldsymbol{V}}(\boldsymbol{p}, \boldsymbol{k})}{\boldsymbol{k}^2}. \tag{44}$$

In Table 6 we list the values of $\hat{V}_4$, $\hat{U}_p$, and $\hat{U}_k$ for all momentum configurations $(\boldsymbol{p}, \boldsymbol{k})$ at $m_Q = 2.6$ and $\kappa = 0.1570$. In this table, we also list the values of q^2 determined with the tree level mass relation (37) for the B meson.

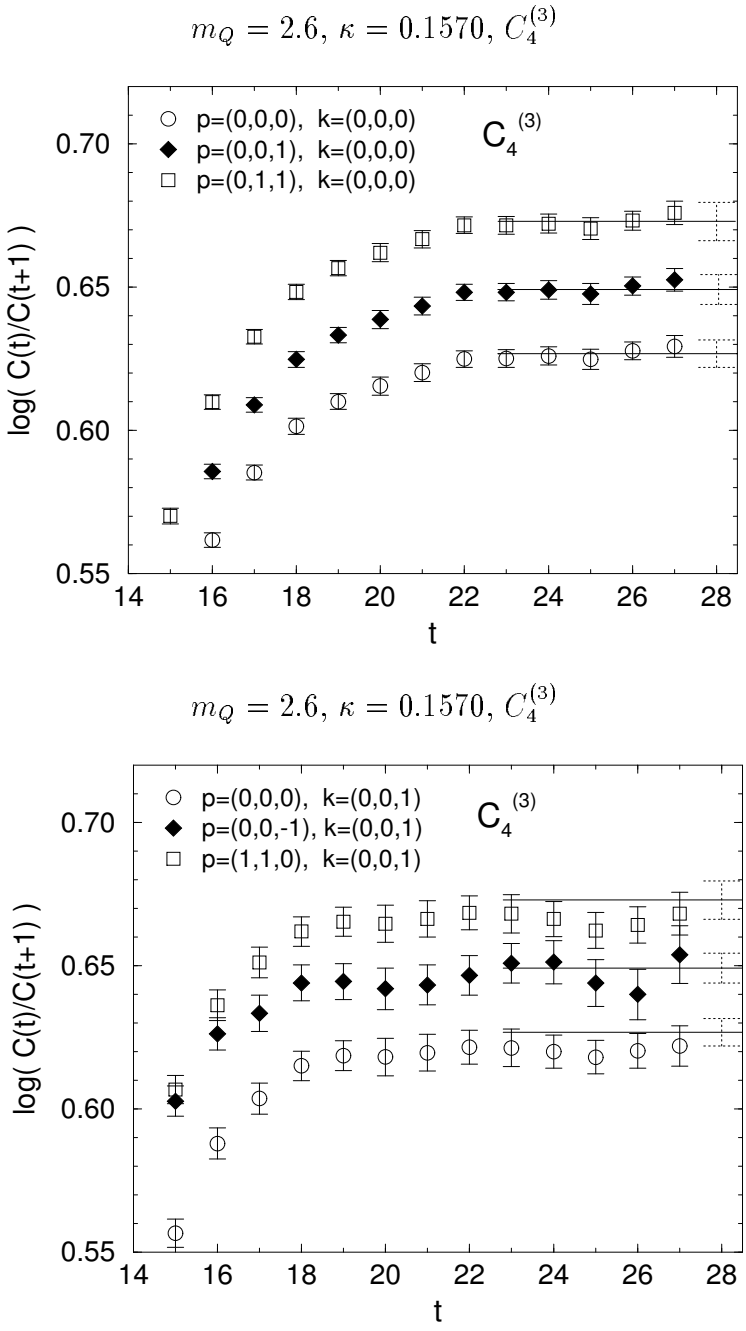

Figure 8: (continued.)

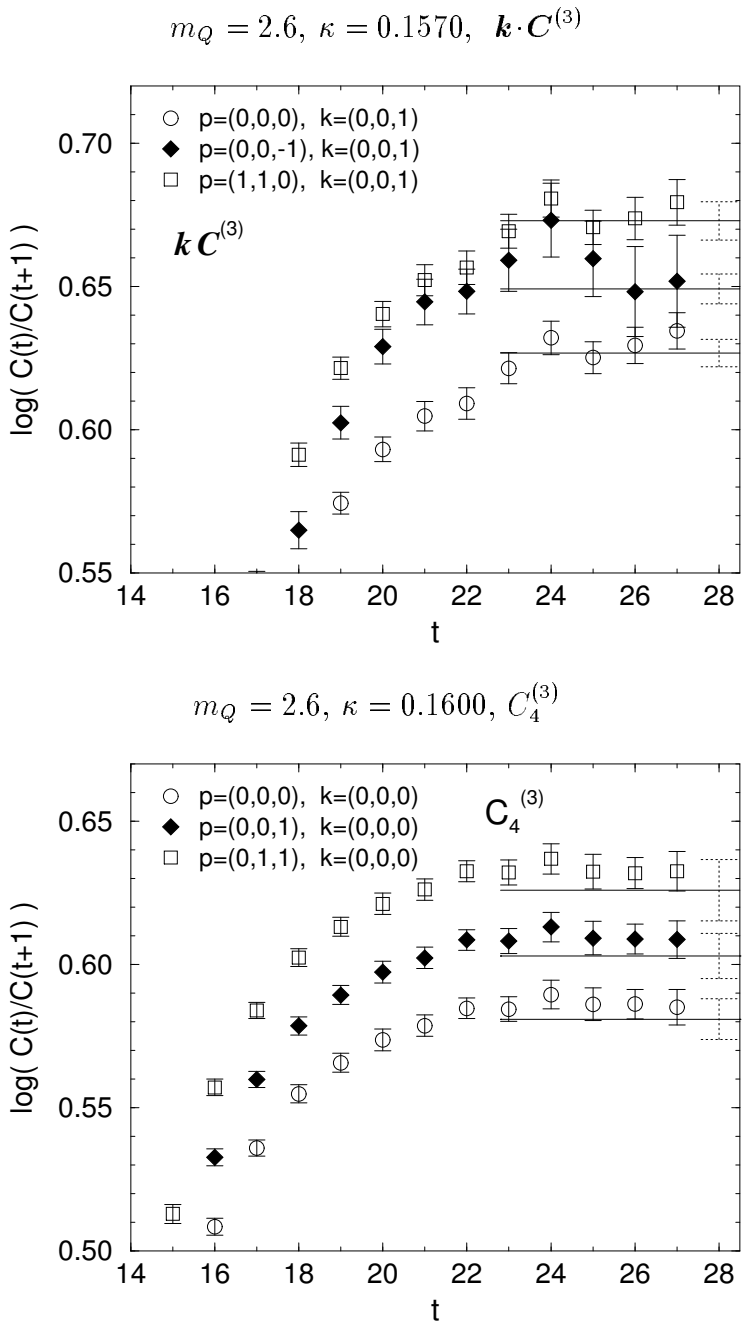

Figure 8: Effective mass plot for the three-point functions at $m_Q = 2.6$ and $\kappa = 0.1570$. The horizontal lines express the values obtained from the two-point correlation functions. Top and middle figures are for $C_4^{(3)}$, and bottom figure is for $\boldsymbol{k}\cdot\boldsymbol{C}^{(3)}$.

We have investigated the n-dependence of $\hat{V}_\mu$ at $m_Q = 2.1$ with $n = 1$ and 2 and at $m_Q = 1.2$ with $n = 2$ and 3, using the first 60 configurations on which $(m_Q, n) = (2.1, 2)$ and $(1.2, 3)$ data are measured[2]. For both of the heavy quark masses we observed small dependence on n, which is at most 1%, 8% and 2% for $\hat{V}_4$, $\hat{U}_p$ and $\hat{U}_k$ respectively, and smaller than their statistical error. In the present work, therefore, we regard them to be sufficiently small to estimate the size of the renormalization effect in the manner described in Section 2.3.

3.5 Form factors

To convert $\hat{V}_4$, $\hat{U}_p$, and $\hat{U}_k$ to the form factors, we need to assume certain dispersion relations for $E_B(\boldsymbol{p})$ and $E_\pi(\boldsymbol{k})$. One method is to use the values obtained from the dispersion relation measured in the simulation. This, however, suffers from the large statistical error for the finite spatial momenta. Alternatively, we adopt the following relativistic dispersion relations for both the B meson and the pion.

$$E_B(\boldsymbol{p}) = \sqrt{m_B^2 + \boldsymbol{p}^2}, \qquad E_\pi(\boldsymbol{k}) = \sqrt{m_\pi^2 + \boldsymbol{k}^2}, \tag{45}$$

where the measured rest mass is used for m_π and m_B. These relations well reproduce the measured data as shown in Figs. 5 and 7 for light-light and heavy-light mesons, respectively.

Using the relations Eq. (45), the form factors are easily constructed from $\hat{V}_\mu$. First, we calculate $f^0(q^2)$ with

$$f^0(q^2) = \frac{\sqrt{2E_B(\boldsymbol{p})}\sqrt{2E_\pi(\boldsymbol{k})}}{m_B^2 - m_\pi^2}\, q^\mu \hat{V}_\mu, \tag{46}$$

and $f^+(q^2)$ is similarly obtained from $(p+k)^\mu \hat{V}_\mu$ substituting the value of f^0 determined above.

For $\boldsymbol{p} \neq 0$ and $\boldsymbol{k} \neq 0$, f^0 and f^+ are not uniquely determined from $\hat{V}_4$, $\hat{U}_p$, and $\hat{U}_k$. In this case there is an additional relation among $\hat{V}_\mu$'s, which should be satisfied when the Lorentz symmetry is restored. For $\boldsymbol{p} \perp \boldsymbol{k}$ this relation reads

$$E_B(\boldsymbol{p})\hat{U}_p + E_\pi(\boldsymbol{k})\hat{U}_k = \hat{V}_4. \tag{47}$$

[2]We note that n-dependence should be studied on the same configurations. In some of the figures, there appear large deviations for the data with different n but the same m_Q. However, in these graphs only the results for $(m_Q, n) = (2.1, 2), (1.2, 3)$ are obtained from the first 60 configurations and the results for the other combinations of (m_Q, n) are obtained from the entire 120 configurations. It seems that these large deviations seem to arise from the statistical fluctuation caused by the remaining 60 configurations for which there is no the data with $(m_Q, n) = (2.1, 2), (1.2, 3)$.

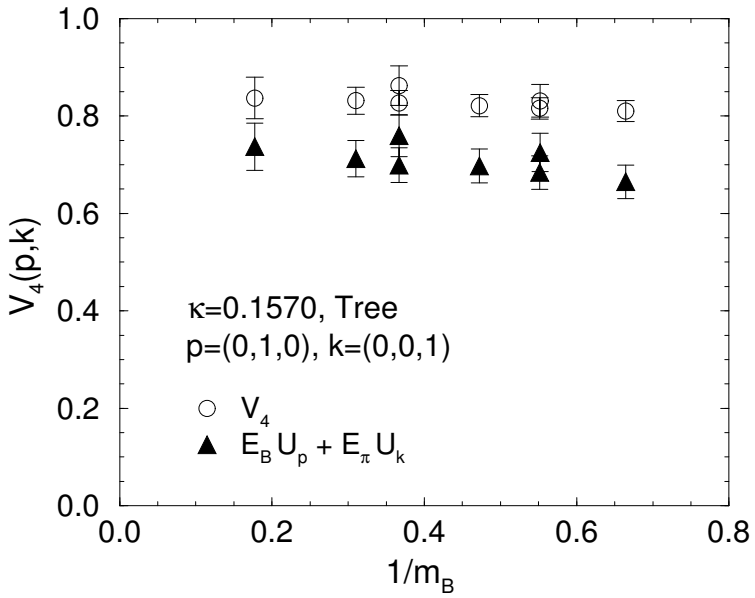

Figure 9: Comparison of $\hat{V}_4$ to ($E_B\hat{U}_p + E_\pi\hat{U}_k$) for $i_q = 6$ at $\kappa = 0.1570$.

We examine this condition for $i_q = 6, 9, 14$ and 16 (i_q is referred in Table 4). Figure 9 compares LHS and RHS of Eq. (47) at $\kappa = 0.1570$ for i_q=6, with the tree level dispersion relation for E_B. This figure exhibits a difference of about 15%. In other cases of i_q, similar amount of the discrepancy is observed. The size of this systematic effect is consistent with the naive expectation for $O(a)$ error.

3.6 Chiral extrapolation

To obtain the form factors at the physical pion and B meson masses, it is necessary to extrapolate the results to the chiral limit. There is, however, still a subtlety in the chiral extrapolation, because the light quark mass dependence of the matrix elements or the form factors are not well understood. In principle, the chiral limit of the matrix elements or the form factors must be taken using the result of the chiral effective theory as a guide for its functional form. For the $B \to \pi$ semileptonic decay the heavy meson effective theory with chiral Lagrangian gives such an example [8, 9, 10].

At least the heavy meson effective theories tell us that the matrix elements or the form factors depend on $v \cdot k$, where v^μ is the 4-velocity of the B meson. At the zero pion momentum, the quantity $v \cdot k$ could potentially give linear dependence in m_π, which could result in a $\sqrt{m_q}$ dependence. The zero recoil limit in the heavy meson effective

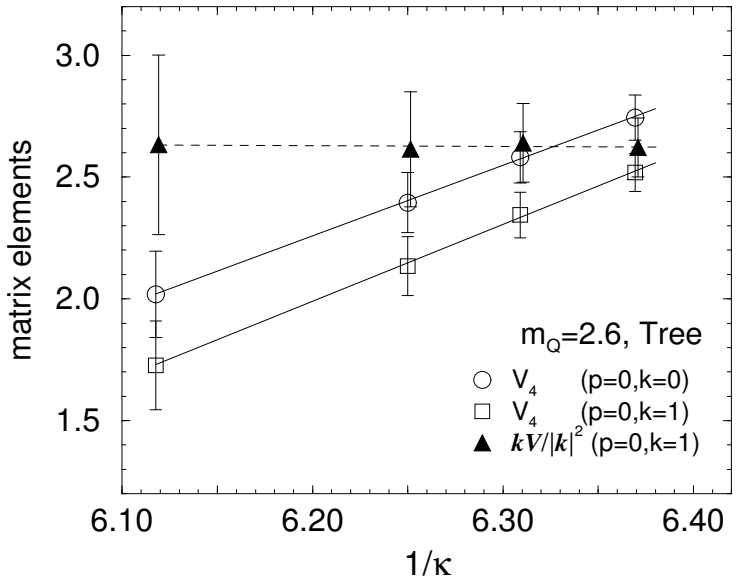

Figure 10: Chiral extrapolation of the matrix elements for $m_Q = 2.6$. V_4 and $\boldsymbol{k} \cdot \boldsymbol{V}/|\boldsymbol{k}|^2$ are shown for two momentum configurations $i_q = 1$, 2. The solid and the dashed lines represent the linear fit.

theory gives the following relations for the matrix element and the form factor:

$$\langle \pi(\boldsymbol{k}=0)|V_4|B(\boldsymbol{p}=0)\rangle = (m_B + m_\pi) f^0(q^2_{\rm max}) = m_B \frac{f_B}{f_\pi}, \tag{48}$$

Assuming the linear dependence of f_B, f_π, and m_B on m_q, at least in the zero recoil limit the matrix element should have linear dependence on m_q. In the following analysis, we take the chiral limit of the matrix elements assuming the linear dependence on m_q in any case of $(\boldsymbol{p}, \boldsymbol{k})$, although there is no proof.

Figure 10 shows the chiral extrapolation of the matrix element with the form

$$\langle \pi(\boldsymbol{k})|V_\mu|B(\boldsymbol{p})\rangle = a_V + b_V m_q, \tag{49}$$

where $m_q = 1/2\kappa - 1/2\kappa_c$. The data itself do not show any sign of nonlinear behavior at least around the strange quark mass. The form factors $f^+(q^2)$ and $f^0(q^2)$ at the physical pion mass are extracted after extrapolating the matrix elements to the chiral limit using Eq.(49).

4 RESULTS AND PHYSICAL IMPLICATIONS

In this section we discuss the physical implications of our results, which include the $1/m_B$ dependence of the $B \to \pi$ matrix elements and the q^2 dependence of the form factors. The prediction from the soft pion theorem is compared with our data.

4.1 $1/m_B$ dependence

The heavy quark effective theory predicts that the properly normalized $B \to \pi$ matrix element has a static limit, hence it can be described by an expansion in the inverse heavy meson mass $1/m_B$ whose leading order is a function of the heavy meson velocity $v_\mu = p_\mu/m_B$,

$$\frac{\langle \pi(\boldsymbol{k})|V_\mu^\dagger|B(\boldsymbol{p})\rangle}{\sqrt{m_\pi m_B}} = \theta_1(v\cdot k)v_\mu + \theta_2(v\cdot k)\frac{k_\mu}{v\cdot k}. \tag{50}$$

Similar arguments for the heavy-light decay constant suggested that the quantity $f_B\sqrt{m_B}$ has the static limit while numerical simulations have shown that the $1/m_B$ correction is very large. On the other hand, the $1/m_B$ dependence of the form factors have been studied only in the D meson region. Therefore it is important to study the $1/m_B$ dependence of the matrix elements at fixed values of $v\cdot k$.

Except for $\boldsymbol{p}=0$, fixing $\boldsymbol{p}$ is not quite identical to fixing $v\cdot k$, since the velocity v_μ changes depending on the heavy meson mass. Thus it is awkward to use the matrix elements with nonzero $\boldsymbol{p}$. In the special case of $\boldsymbol{p}=0$, LHS of Eq. (50) is nothing but the matrix elements $\hat{V}_4$, $\hat{U}_p$ and $\hat{U}_k$, defined in Eqs. (43), and (44), multiplied by the m_B independent factor.

In the following analysis, we confine ourselves to examine the following quantities for the sake of simplicity:

$$\hat{V}_4(\boldsymbol{p}=0,\boldsymbol{k}) = \hat{V}_4^{(0)}\left(1+\frac{c_4^{(1)}}{m_B}+\frac{c_4^{(2)}}{m_B^2}+\cdots\right), \tag{51}$$

$$\hat{U}_k(\boldsymbol{p}=0,\boldsymbol{k}) = \hat{U}_k^{(0)}\left(1+\frac{c_k^{(1)}}{m_B}+\frac{c_k^{(2)}}{m_B^2}+\cdots\right), \tag{52}$$

$$\hat{U}_p(\boldsymbol{p}=0,\boldsymbol{k}) \equiv \lim_{\boldsymbol{p}^2\to 0}\hat{U}_p(\boldsymbol{p},\boldsymbol{k}) \tag{53}$$

$$= \frac{1}{m_B}\hat{U}_p'^{(0)}\left(1+\frac{c_p^{(1)}}{m_B}+\frac{c_p^{(2)}}{m_B^2}+\cdots\right), \tag{54}$$

for which we explicitly show the form of the $1/m_B$ expansion. All of the coefficients in these expansions are a function of $\boldsymbol{k}$.

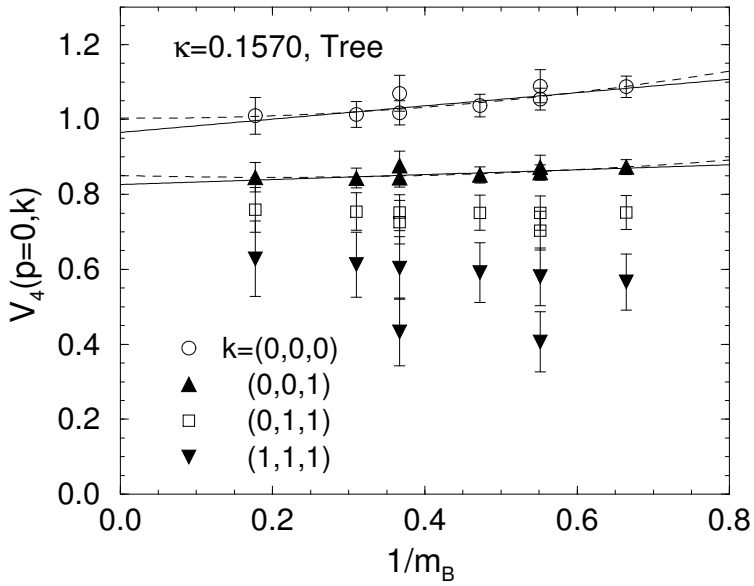

Figure 11: $\hat{V}_4$ at $\kappa = 0.1570$. For $\boldsymbol{k} = 0$ and $|\boldsymbol{k}| = 1$, the solid and the dashed lines represent the results of linear and quadratic fits, respectively.

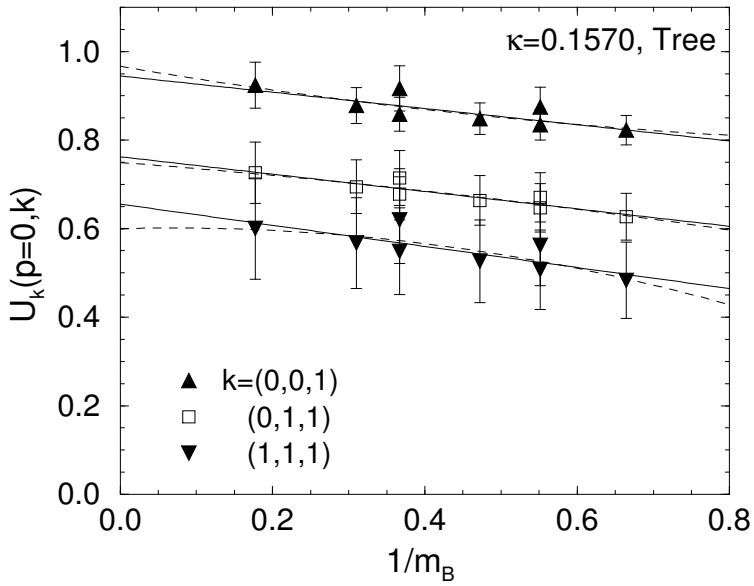

Figure 12: $\hat{U}_k$ at $\kappa = 0.1570$. The solid and the dashed lines represent the results of linear and quadratic fits, respectively.

In Figs. 11 and 12 we show the $1/m_B$ dependence of $\hat{V}_4$ and $\hat{U}_k$, respectively, at $\kappa = 0.1570$. The $1/m_B$ correction is not significant for these quantities and almost negligible around the B meson mass. This result exhibits a sharp contrast to the mass dependence of the heavy-light decay constant $f_B\sqrt{m_B}$, for which the large $1/m_B$ correction to the static limit is observed. Results of the linear and quadratic fit in $1/m_B$ are listed in Table 7 for $\hat{V}_4$ and in Table 8 for $\hat{U}_k$.

		linear		quadratic		
κ	i_q	$\hat{V}_4^{(0)}$	$c_4^{(1)}$	$\hat{V}_4^{(0)}$	$c_4^{(1)}$	$c_4^{(2)}$
0.1570	1	0.965(35)	0.184(55)	1.003(47)	−0.01(20)	0.21(18)
	2	0.826(29)	0.080(47)	0.851(41)	−0.06(17)	0.15(17)
	3	0.757(51)	−0.038(59)	0.799(57)	−0.30(20)	0.31(22)
	4	0.624(80)	−0.25 (11)	0.79 (10)	−1.29(36)	1.25(42)
0.1585	1	0.982(42)	0.165(63)	1.016(55)	−0.00(23)	0.18(21)
	2	0.807(35)	0.075(57)	0.830(48)	−0.06(20)	0.14(19)
	3	0.758(76)	−0.071(73)	0.830(81)	−0.51(26)	0.51(29)
	4	0.62 (12)	−0.40 (15)	0.89 (19)	−1.83(50)	1.75(60)
0.1600	1	1.003(53)	0.150(76)	1.023(66)	0.05(27)	0.10(25)
	2	0.768(46)	0.088(76)	0.788(58)	−0.04(26)	0.14(25)
	3	0.78 (14)	−0.17 (10)	0.96 (17)	−1.13(40)	1.13(46)
	4	0.70 (27)	−0.64 (25)	1.22 (55)	−2.45(80)	2.26(94)

Table 7: Parameters for the linear and quadratic fits of $\hat{V}_4(\boldsymbol{p} = 0, \boldsymbol{k})$.

		linear		quadratic		
κ	i_q	$\hat{U}_k^{(0)}$	$c_k^{(1)}$	$\hat{U}_k^{(0)}$	$c_k^{(1)}$	$c_k^{(2)}$
0.1570	2	0.945(39)	−0.194(44)	0.967(47)	−0.30(19)	0.13(19)
	3	0.762(56)	−0.257(53)	0.750(54)	−0.17(22)	−0.10(24)
	4	0.655(88)	−0.364(91)	0.600(81)	0.08(43)	−0.54(49)
0.1585	2	1.004(52)	−0.198(50)	1.023(58)	−0.28(22)	0.10(23)
	3	0.808(92)	−0.242(64)	0.769(80)	0.00(30)	−0.29(32)
	4	0.72 (15)	−0.34 (14)	0.58 (12)	0.77(74)	−1.34(80)
0.1600	2	1.064(73)	−0.214(62)	1.063(77)	−0.21(29)	0.00(30)
	3	0.92 (20)	−0.219(90)	0.80 (16)	0.47(50)	−0.81(53)
	4	0.94 (37)	−0.23 (26)	0.55 (23)	3.3 (23)	−4.1 (24)

Table 8: Parameters for the linear and quadratic fits of $\hat{U}_k(\boldsymbol{p} = 0, \boldsymbol{k})$.

We note here that χ^2/dof are less than unity for most cases of V_4, U_k, and also U_p, which will be mentioned in the next paragraph, though they do not exactly judge the goodness of the fits for such data, which are correlated for different m_Q.

In order to do the same discussion for $\hat{U}_p$, which is defined in the $\boldsymbol{p}^2 \to 0$ limit, we extrapolate the finite $\boldsymbol{p}$ results to the vanishing $\boldsymbol{p}$ point as shown in Fig. 13. There is little $\boldsymbol{p}^2$ dependence observed and we employ a linear extrapolation in $\boldsymbol{p}^2$. In Fig. 14 we plot $m_B\hat{U}_p$ as a function of $1/m_B$ at $\kappa = 0.1570$. In contrary to the other matrix elements we observe a sizable $1/m_B$ dependence. Table 9 summarizes the results of linear and quadratic fit of $m_B\hat{U}_p$.

Here we briefly discuss the effect of one-loop correction to these quantities. Figure 15 shows the renormalized values of $\hat{V}_4(i_q = 1)$, $\hat{U}_k(i_q = 2)$, and $m_B\hat{U}_p(i_q = 1)$ at $\kappa = 0.1570$. As mentioned at the end of Section 2, the leading logarithmic factor is multiplied to $\hat{V}_\mu$. As mentioned at the end of Section 2, the leading logarithmic factor Eq. (36) is multiplied to $\hat{V}_\mu$. We also list the results of linear fits of them in Table 10. As we discussed previously, the $1/m_Q$ dependence of the one-loop coefficient is significant

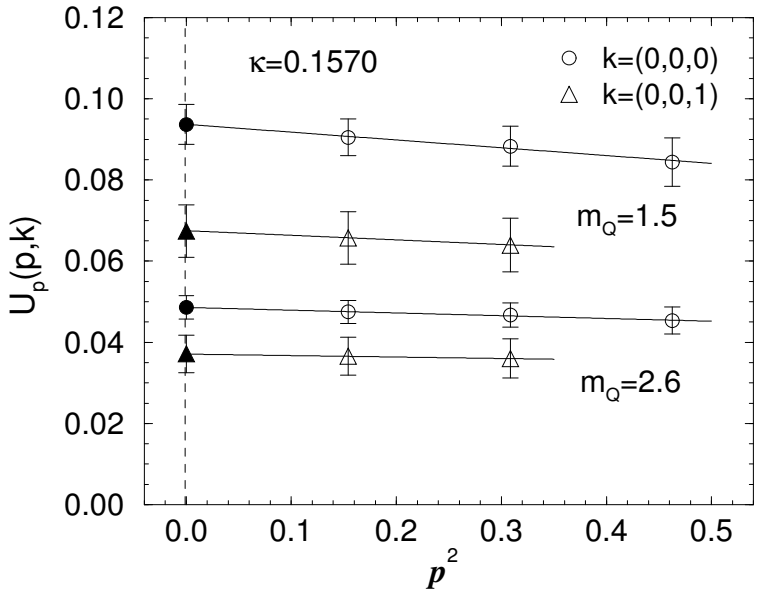

Figure 13: Extraction of $\hat{U}_p(\boldsymbol{p}=0,\boldsymbol{k})$ is shown for $m_Q = 2.6$ and 1.5 at $\kappa = 0.1570$. The extrapolation is carried out linearly in $\boldsymbol{p}^2$. For $\boldsymbol{k} = 0$, $i_q = 5, 13, 20$ are used. For $\boldsymbol{k} = 1$, $\hat{U}_p(0,\boldsymbol{k})$ is determined using $i_q = 6, 14$, for which $\boldsymbol{p}$ and $\boldsymbol{k}$ are perpendicular.

only for V_4 and almost negligible for V_i. As a result, the $1/m_B$ dependence of $\hat{V}_4$ is largely affected by the renormalization effect, and it even changes the sign of the slope in $1/m_B$. The $1/m_B$ dependence of $\hat{V}_4$ is still mild after the renormalization effect is included. For $\hat{U}_k$ and $m_B\hat{U}_p$ the $1/m_B$ dependence is not affected by the one-loop correction, while their amplitudes decrease by at most 30%.

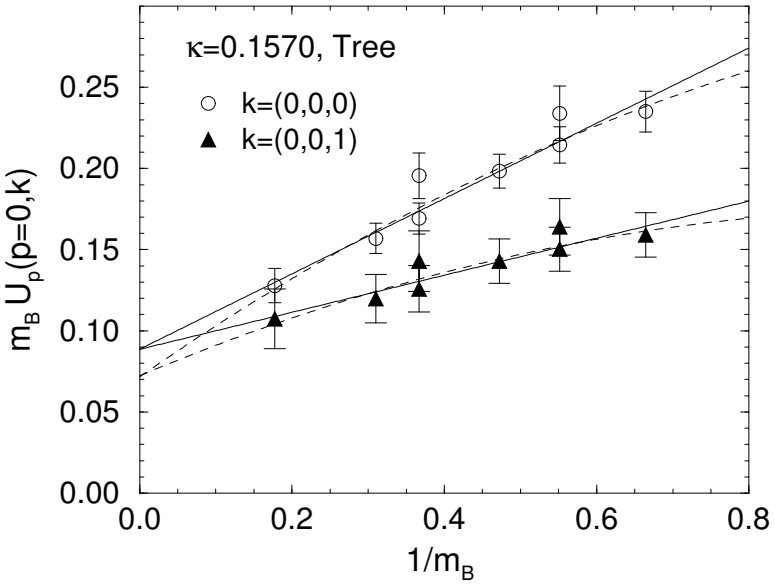

Figure 14: $\hat{U}_p$ multiplied by m_B at $\kappa = 0.1570$ as a function of $1/m_B$. The values of m_B are determined with the tree level formula. The solid and the dashed lines represent the linear and the quadratic fits, respectively.

		linear		quadratic		
κ	i_q	$\hat{U}_p'^{(0)}$	$c_p^{(1)}$	$\hat{U}_p'^{(0)}$	$c_p^{(1)}$	$c_p^{(2)}$
0.1570	1	0.0887(80)	2.61(39)	0.0717(95)	4.5(12)	−1.55(76)
	2	0.089 (14)	1.29(38)	0.072 (13)	2.7(11)	−1.31(88)
0.1585	1	0.0872(94)	2.65(47)	0.066 (11)	5.3(17)	−2.1 (10)
	2	0.093 (20)	0.98(42)	0.080 (18)	2.0(12)	−1.0 (11)
0.1600	1	0.088 (12)	2.72(59)	0.059 (15)	6.7(27)	−3.1 (17)
	2	0.104 (33)	0.67(47)	0.097 (27)	1.1(15)	−0.4 (15)

Table 9: Parameters for the linear and quadratic fits of $\hat{U}_p(\boldsymbol{p} = 0, \boldsymbol{k})$.

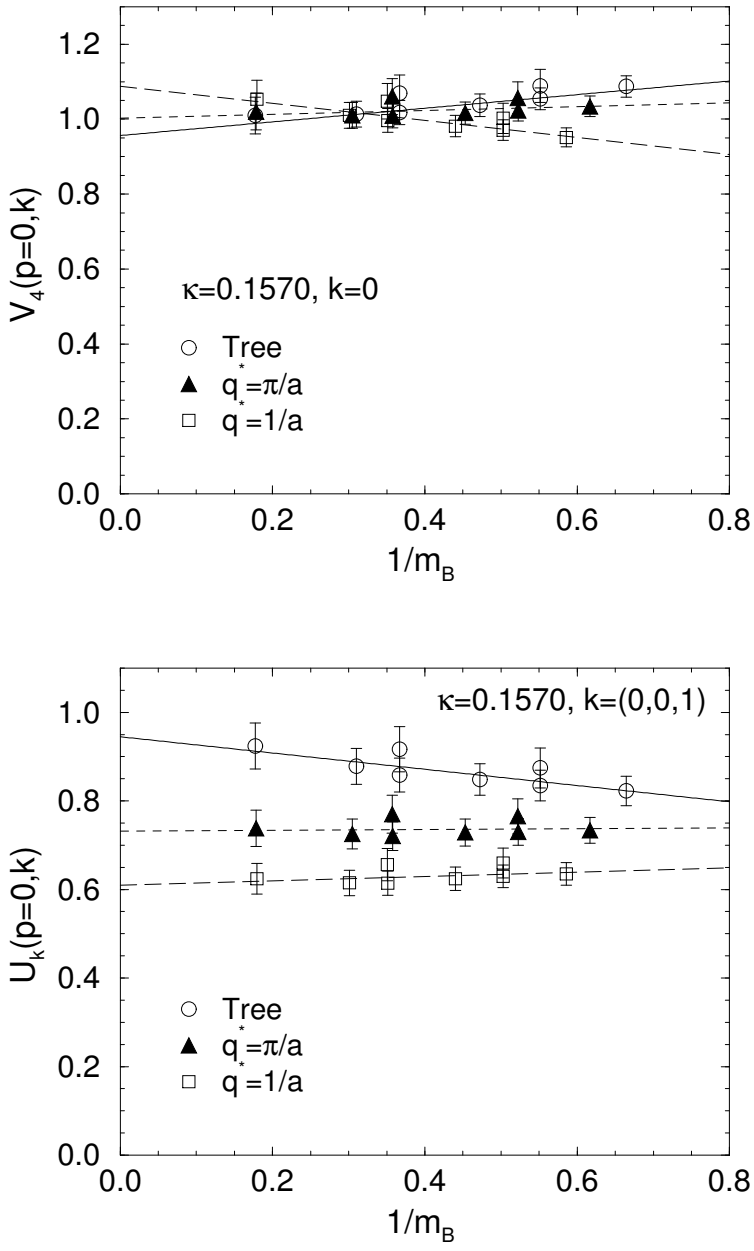

Figure 15: (continued.)

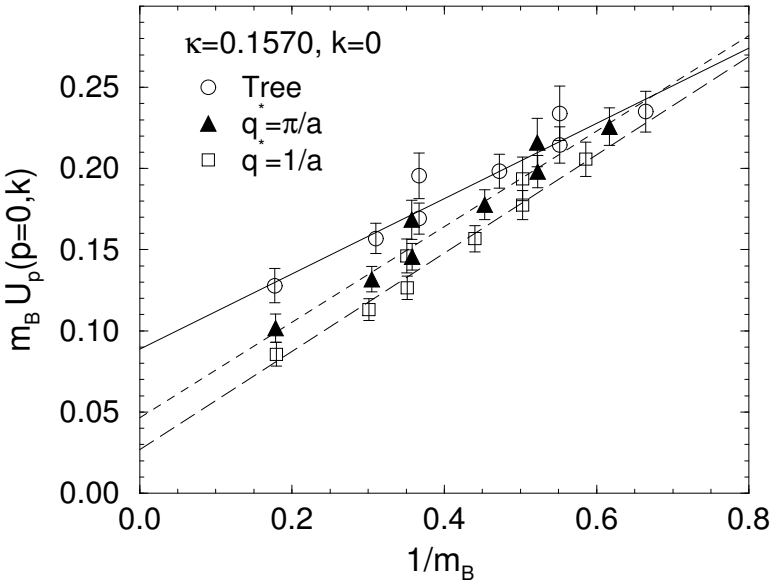

Figure 15: One-loop renormalized $\hat{V}_4$, $\hat{U}_k$, and $\hat{U}_p$ as a function of $1/m_B$. The solid, the dashed, and the long dashed lines represent the linear fits.

$\hat{V}_4(\boldsymbol{p}=0,\boldsymbol{k}=0)$ ($i_q=1$)

	$q^*=\pi/a$		$q^*=1/a$	
κ	$V_4^{(0)}$	$c_4^{(1)}$	$V_4^{(0)}$	$c_4^{(1)}$
0.1570	1.002(36)	0.052(55)	1.088(39)	−0.209(47)
0.1585	1.019(44)	0.039(63)	1.105(46)	−0.216(55)
0.1600	1.039(55)	0.030(77)	1.126(58)	−0.219(66)

$\hat{U}_k(\boldsymbol{p}=0,|\boldsymbol{k}|=1)$ ($i_q=2$)

	$q^*=\pi/a$		$q^*=1/a$	
κ	$\hat{U}_k^{(0)}$	$c_k^{(1)}$	$\hat{U}_k^{(0)}$	$c_k^{(1)}$
0.1570	0.732(31)	0.013(61)	0.609(27)	0.081(70)
0.1585	0.778(42)	0.005(68)	0.649(36)	0.070(78)
0.1600	0.826(59)	−0.019(84)	0.689(50)	0.043(96)

$\hat{U}_p(\boldsymbol{p}=0,\boldsymbol{k}=0)$ ($i_q=1$)

	$q^*=\pi/a$		$q^*=1/a$	
κ	$\hat{U}_p^{(0)}$	$c_p^{(1)}$	$\hat{U}_p^{(0)}$	$c_p^{(1)}$
0.1570	0.0466(66)	6.3(12)	0.0268(58)	11.3(30)
0.1585	0.0453(77)	6.5(15)	0.0256(68)	11.8(38)
0.1600	0.045 (10)	6.7(19)	0.0248(87)	12.5(53)

Table 10: Parameters for the linear fit of the renormalized matrix elements $\hat{V}_4(\boldsymbol{p}=0,\boldsymbol{k}=0)$, $\hat{U}_k(\boldsymbol{p}=0,|\boldsymbol{k}|=1)$, and $\hat{U}_p(\boldsymbol{p}=0,\boldsymbol{k}=0)$.

4.2 q^2-dependence of the form factors

First we study for which q^2 region our present statistics allow us to compute the form factors with reasonable statistical errors. The q^2 dependence of the form factors f^+ and f^0 are shown in Figs. 16 and 17 at m_Q=2.6 and 1.5, respectively. We find that for $\kappa = 0.1570 (m_q \sim 2m_s)$, the range of q^2 in which the form factors have good signal covers almost the entire kinematic region for D meson and one third of the kinematic region for B meson. For $\kappa = 0.1600$ ($m_q \sim m_s$), the signal becomes much noisier, but still the form factors have marginally good signal for half and one fourth of the kinematic region for D meson and B meson, respectively. Although our present results are very noisy after the chiral extrapolation, this will be improved by future high statistics studies. This is encouraging in view of the fact that the future B Factories can produce 10^8 B-$\overline{B}$ pairs and the branching fraction of $B \to \pi l \nu$ from CLEO is $(1.8 \pm 0.4 \pm 0.3 \pm 0.2) \times 10^{-4}$ [5]. It is reasonable to expect that there is a possibility of observing $B \to \pi l \nu$ events in the q^2 regime which the present lattice calculation can cope with.

Secondly we study the q^2 dependence to see whether the contribution from the B^* resonance to the form factor can actually be observed in the simulation data. At the chiral limit, unfortunately, the results are too noisy to discuss their q^2 dependence, therefore we use the finite mass results only in the following analysis of the q^2 dependence. As shown in Figs. 16 and 17, the lattice results are available only in the large q^2 region, at which the recoil momentum of pion is small enough. Therefore it is justified to express the functional form of the form factors by an expansion around the zero recoil limit. For this purpose we use the inverse form factors $1/f^+(q^2)$ and $1/f^0(q^2)$:

$$1/f(q^2) = 1/f(q^2_{\rm max}) + c_1(q^2_{\rm max} - q^2) + c_2(q^2_{\rm max} - q^2)^2. \qquad (55)$$

Figure 18 shows the inverse form factors at $m_Q = 2.6$ as well as their fitted functions with this form. The numerical results of the fit with and without the condition $c_2 = 0$ are given in Table 11 for $m_Q = 2.6$, 1.5, and 0.9.

The pole dominance model corresponds to a special case $c_2 = 0$, which seems to describe the data very well as shown in Fig. 18. The mass of the intermediate state is given by $m^2_{\rm pole} = q^2_{\rm max} + 1/(c_1 f^+(q^2_{\rm max}))$, which corresponds to the vector (B^*) meson mass in the pole dominance model. Precisely speaking, the more consistent analysis is to impose the condition $m_{\rm pole} = m_{B^*}$ for the fit by Eq. (55). This constrained fit is shown with the long dashed line in Fig. 18. It is found that now the fit do not quite agree with the data, but the deviation is about 10 %.

In Fig. 19 we also compare $m_{\rm pole}$ and the measured vector meson mass as a function of m_B. Again we find that there is a discrepancy between $m_{\rm pole}$ from the unconstrained fit

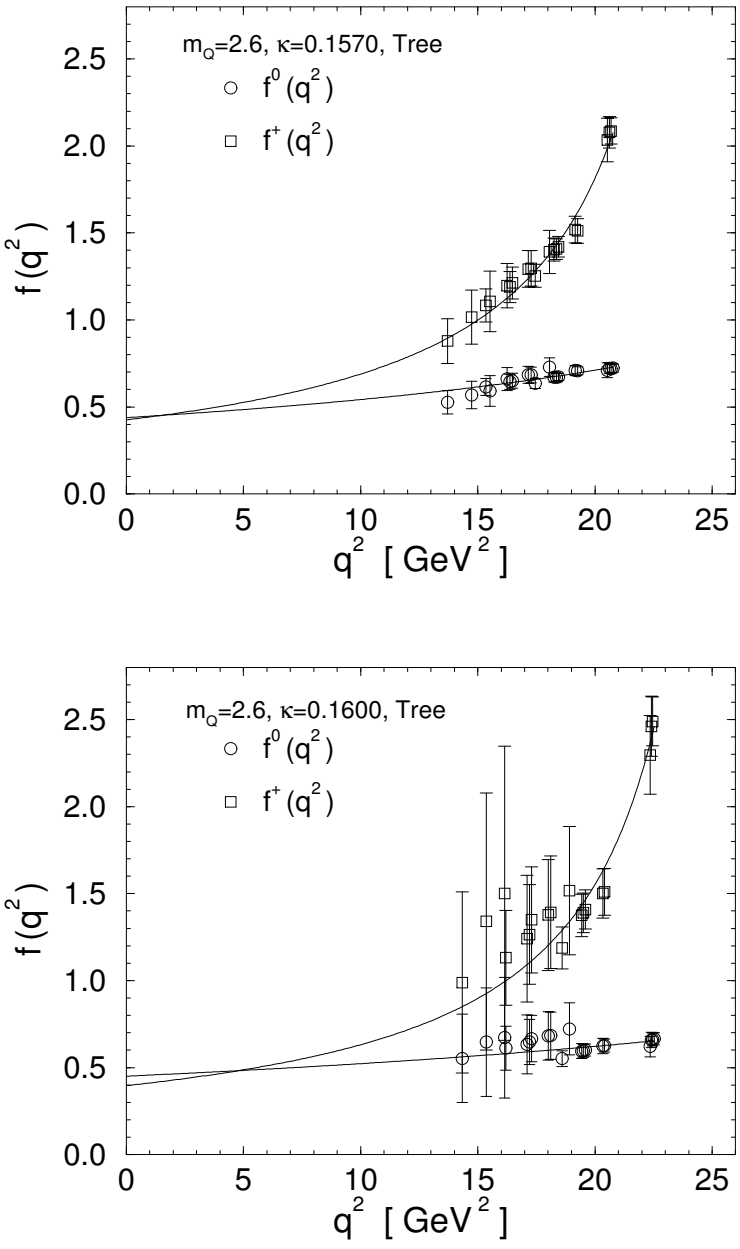

Figure 16: Form factors at $m_Q = 2.6$ and $\kappa = 0.1570, 0.1600$. The solid curves represent the fit to single pole functions.

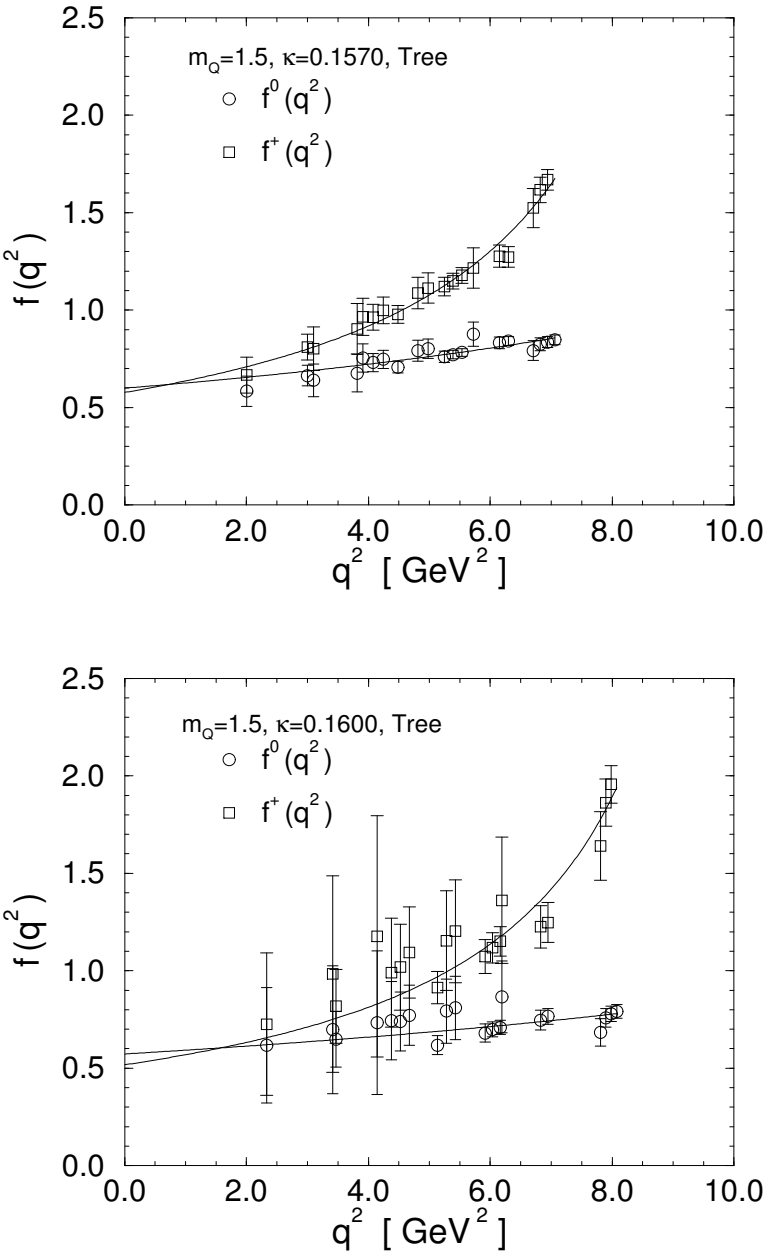

Figure 17: Form factors at $m_Q = 1.5$ and $\kappa = 0.1570, 0.1600$.

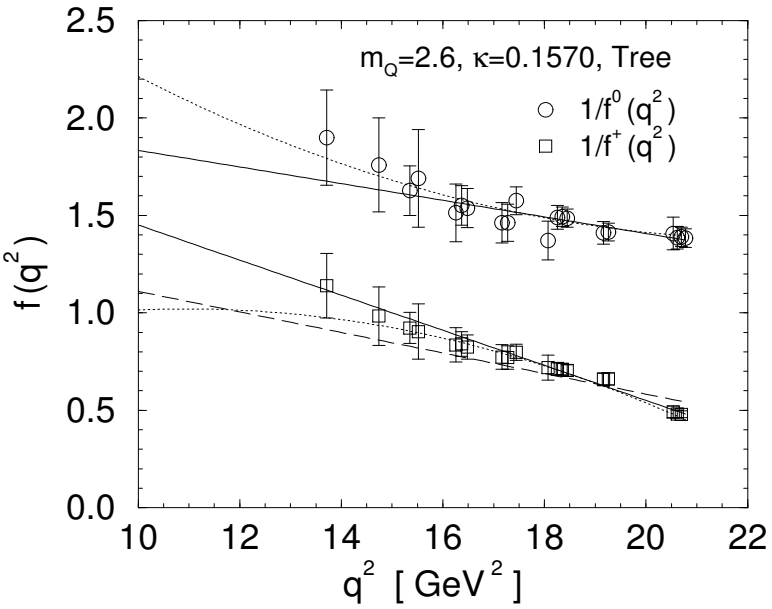

Figure 18: $1/f^0$ and $1/f^+$ as a function of q^2 at $m_Q = 2.6$ and $\kappa = 0.1570$. The solid and the dotted curves represent the linear and the quadratic fits, respectively. The long dashed line represents the linear fit with the constraint $m_{\rm pole} = m_{B^*}$, where m_B^* is the B^* meson mass obtained from the two-point correlation function.

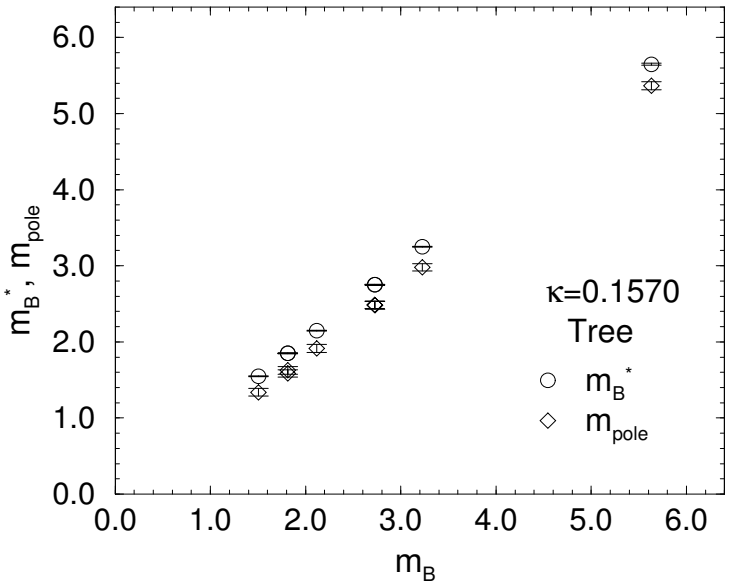

Figure 19: m_{B^*} obtained from the two-point correlation function of the B^* meson and the pole mass from the linear fit of $1/f^+$.

		linear fit		quadratic fit		
(m_Q, n)	κ	$f^{-1}(q^2_{\rm max})$	c_1	$f^{-1}(q^2_{\rm max})$	c_1	c_2
(2.6, 1)	0.1570	1.373(54)	0.126(70)	1.386(52)	0.058(64)	0.046(53)
		0.480(21)	0.264(38)	0.470(20)	0.335(40)	−0.051(37)
	0.1585	1.436(70)	0.109(88)	1.438(64)	0.098(91)	0.007(81)
		0.445(24)	0.272(47)	0.434(22)	0.366(59)	−0.068(54)
	0.1600	1.531(94)	0.09 (11)	1.512(86)	0.22 (16)	−0.09 (14)
		0.407(27)	0.276(61)	0.395(26)	0.44 (10)	−0.115(86)
(1.5 , 2)	0.1570	1.167(38)	0.209(81)	1.185(37)	0.086(80)	0.119(87)
		0.597(25)	0.472(64)	0.587(22)	0.548(60)	−0.075(78)
	0.1585	1.213(50)	0.19 (10)	1.224(47)	0.10 (12)	0.08 (14)
		0.559(28)	0.493(78)	0.545(24)	0.623(92)	−0.13 (12)
	0.1600	1.283(67)	0.17 (14)	1.279(62)	0.21 (20)	−0.04 (24)
		0.516(32)	0.52 (10)	0.496(29)	0.77 (17)	−0.26 (20)
(0.9 , 2)	0.1570	1.011(28)	0.360(88)	1.027(27)	0.208(85)	0.19 (13)
		0.685(28)	0.753(90)	0.690(26)	0.713(75)	0.05 (13)
	0.1585	1.041(36)	0.35 (11)	1.056(35)	0.19 (13)	0.20 (21)
		0.647(33)	0.79 (11)	0.640(28)	0.86 (12)	−0.09 (21)
	0.1600	1.090(49)	0.33 (15)	1.096(48)	0.26 (24)	0.10 (35)
		0.599(37)	0.85 (14)	0.577(32)	1.12 (23)	−0.36 (36)

Table 11: Parameters for the fit $f^{-1}(q^2) = f^{-1}(q^2_{\rm max}) + c_1(q^2_{\rm max} - q^2) + c_2(q^2_{\rm max} - q^2)^2$, where c_2 is set to zero for the linear fit. For each (m_Q, n) and κ, numbers in upper and lower rows correspond f^0 and f^+, respectively. In all the cases, χ^2/dof are less than unity.

and the measured m_{B^*}, which is around few hundred MeV. Nevertheless, it is remarkable that the deviation remains the same order and the mass dependence of $m_{\rm pole}$ has the same trend with m_{B^*}. We have not yet understood whether the above discrepancies can be explained from the remaining systematic errors such as the discretization error. But at least qualitatively judging from the size of the uncertainty in our calculation, our data is not inconsistent with the picture that there is a sizable contribution from the B^* pole to the form factor f^+ near $q^2_{\rm max}$.

So far the discussion have been based on the tree level study. Let us now study how one-loop renormalization changes the form factors. Because the one-loop correction is different for V_4 and V_i, the shape of the form factors may change significantly. Figure 20 shows the form factors for $m_Q = 2.6$ and $\kappa = 0.1570$ with renormalization factors. The leading logarithmic factor Eq.(36) is not multiplied in the present case. We find that the renormalized f^+ has stronger q^2 dependence than that of at the tree level, while f^0

receives only a small change. The renormalization makes the B^* pole fit even worse. In fact, the deviation of the constrained fit from our renormalized f^+ data is as large as 25 % near $q^2_{\rm max}$. This is still within the typical size of $O(a)$ errors. It is very important to perform the analysis with larger β.

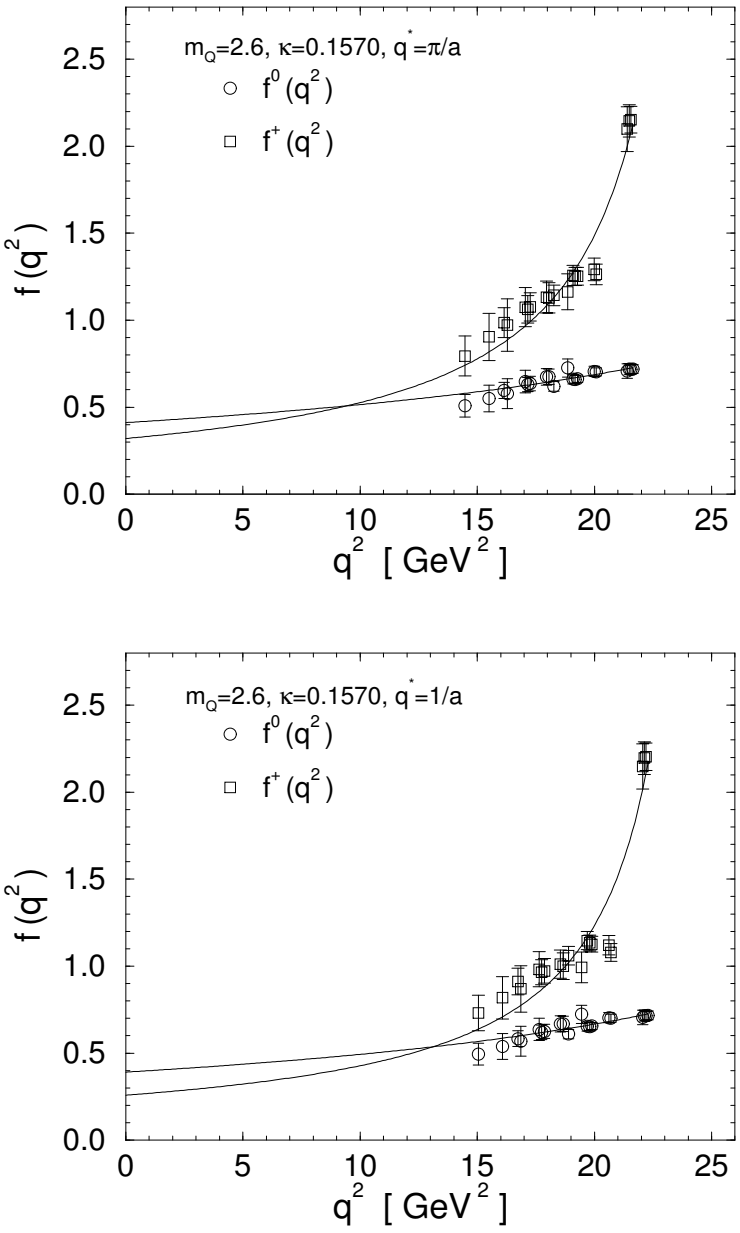

Figure 20: Renormalized form factors at $m_Q = 2.6$ and $\kappa = 0.1570$. Upper and lower figures are obtained with $g_V^2(\pi/a)$ and $g_V^2(1/a)$, respectively. The solid lines represent the results of the linear fit. For $f^+(q^2)$, χ^2/dof are 1.9 and 4.1 for $q^* = \pi/a$ and $1/a$ respectively. χ^2/dof for $f^0(q^2)$ are less than 0.5 in the both cases.

4.3 Soft pion theorem

Applying the soft pion theorem to the $B \to \pi$ matrix element, $f^0(q^2_{\rm max})$ is related to the B meson decay constant [9, 10, 11]

$$f^0(q^2_{\rm max}) = f_B/f_\pi. \tag{56}$$

in the massless pion limit. This relation is examined in Fig. 21. For the values of f_B, we refer our work on f_B[30], which is obtained with an evolution equation of a slightly different form from that of the present work. We observe a large discrepancy between f^0 and the decay constant both for the $1/m_B$ dependence and for the value itself. f_B increases rapidly toward heavier heavy quark masses, while $f^0(q^2_{\rm max})$ almost stays constant.

The discrepancy still remains significant when the renormalization effect is incorporated. In evaluating the renormalized values of f_B, we use one-loop perturbative coefficient obtained in the same manner as in Section 2.3 [31]. The leading logarithmic factor Eq.(36) is multiplied to both $f^0(q^2_{\rm max})$ and f_B.

One may argue that the observed discrepancy can be explained by the uncertainty in

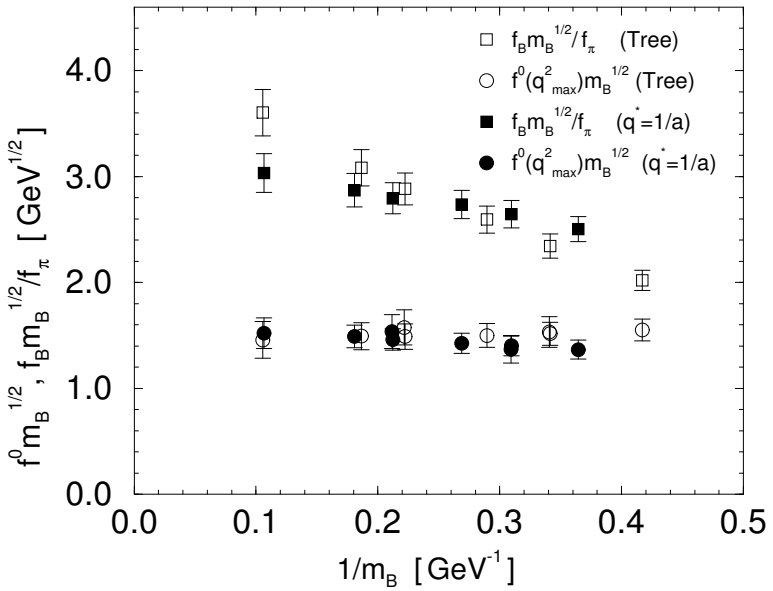

Figure 21: Comparison of $f^0(q^2_{\rm max})$ with f_B/f_π multiplying the factor $\sqrt{m_B}$ in the chiral limit. Open and filled symbols are at the tree level and at the one-loop with $g^2_V(1/a)$, respectively.

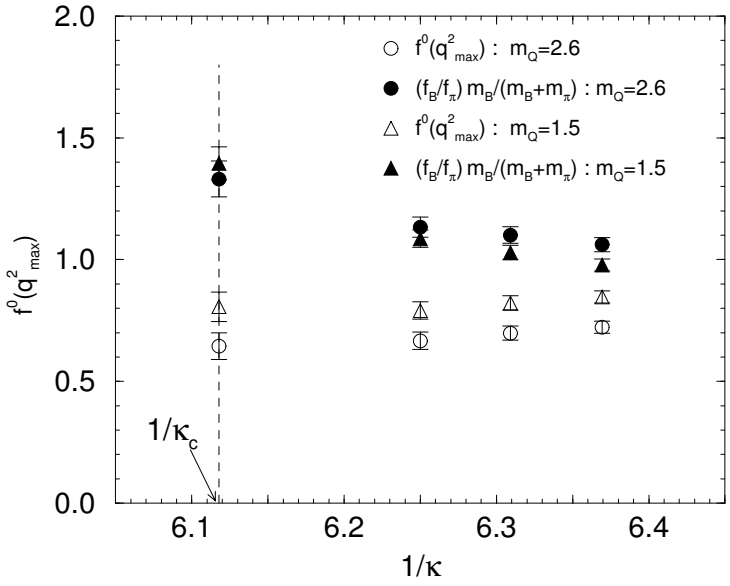

Figure 22: $f^0(q^2_{\rm max})$ and $(f_B/f_\pi)m_B/(m_B+m_\pi)$ for light quark masses. Two cases of m_Q, 2.6 and 1.5, are displayed at the tree level.

the extrapolation procedure. To study this possibility, we compare $f^0(q^2_{\rm max})$ and f_B/f_π also in finite light quark mass cases, in the light of the heavy meson effective theory which implies the relation (48). They are compared in Fig. 22 as a function of $1/\kappa$. The difference between them are remarkable even for finite light quark mass cases.

The reason why these differences occur is not clear. Since our present results suffer from various systematic uncertainties, as described in the next section, further study with better control of systematic errors is necessary to clarify the origin of the problem.

5 EXAMINATION OF SYSTEMATIC ERRORS

In this section, we qualitatively discuss on the systematic uncertainties associated with the lattice regularization. The following is a list of the main sources of systematic errors:

- $O(a)$ errors: The characteristic size of $O(a\Lambda_{QCD})$ error arising from the unimproved Wilson quark action at $\beta = 5.8$ is 20–30%. This effect is large enough to explain the discrepancy between $E_B(\boldsymbol{p})\hat{U}_p + E_\pi(\boldsymbol{k})\hat{U}_k$ and $\hat{V}_4$, mentioned in Section 3. Use of the $O(a)$-improved Clover action for the light quark will reduce this error to the level of 5 %.

- $O(ap)$ error: The systems with finite momentum may suffer from the discretization errors more seriously than that at the zero recoil point. The analytic estimate of the momentum dependent error [12] shows that the effect is about 20 % at $|\boldsymbol{p}| \sim 1$ GeV even one uses the $O(a)$-improved current. In general, the use of the Wilson action for the light quark could introduce such a error of order $O(ap)$ in practical nonperturbative case.

- Perturbative corrections: The one-loop correction could become significant especially for small β values. Strictly speaking, our calculation does not treat the one-loop effects correctly, because the stabilizing parameter n does not have correct values. This problem must be removed in the future studies. In estimating the one-loop corrections, we did not include the effect of the operator mixing, which was reported to be significant in the case of f_B [33]. This effect also should be included to obtain reliable results.

- $O(1/m_Q^2)$ effects: We described the heavy quark with the NRQCD action including the order $1/m_Q$ terms. Further precise calculations may need to include $O(1/m_Q^2)$ corrections, although the effect was shown to be small[30, 32] for f_B.

The finite volume effect may also be important.

Since the all above systematic errors can be large, there is no advantage of giving quantitative estimates of each error at this stage. The use of the $O(a)$-improved (clover) action for light quark, as well as the simulation at higher β values will reduce most of the above systematic errors. The simulation with dynamical quarks is also of great importance for reliable predictions of the weak matrix elements.

6 CONCLUSION

In this paper, we present the results of the study of $B \to \pi$ form factors using NRQCD to describe the heavy quark with the Wilson light quark. Clear signal is observed for the matrix element in a wide range of heavy quark mass containing the physical b-quark mass. They are extrapolated to the chiral limit, although the result is so noisy for quantitative conclusion.

The $1/m_B$ dependence of the matrix elements are studied and it is clarified that the temporal component and the part of the spatial component proportional to the pion momentum have fairly small dependencies on m_Q. On the other hand, the part of the spatial component proportional to the B momentum has a significant $O(1/m_B)$ correction.

The q^2 dependence of the form factors in the finite light quark masses are studied. We find that the q^2 dependence of the form factor $f^+(q^2)$ near $q^2_{\rm max}$ becomes much stronger for larger heavy quark mass. Model independent fit of $1/f^+(q^2)$ near $q^2_{\rm max}$ shows that the tree level results are consistent with the pole behavior for large q^2 range, and the difference of fitted pole mass and the measured m_{B^*} is around few hundred MeV for all the heavy quark masses.

The values of f^0 at the zero recoil point are compared with the prediction of the soft pion theorem, and the significant discrepancy is observed.

The size of the renormalization corrections are estimated by the one-loop perturbative calculation. They almost does not affect their $1/m_Q$ dependence, but decrease V_i much more than V_4, which drastically change the shape of f^+. Our present result suffers from large systematic uncertainties, and the most important one is $O(a)$ error. It is very important to study at higher β with improved actions.

ACKNOWLEDGMENT

This study has done in collaboration with *Shoji Hashomoto* of High Energy Accelerator Research Organization (KEK) (now he stays at Fermi National Accelerator Laboratory in U.S.A.), *Tetsuya Onogi, Ken-Ichi Ishikawa*, and *Norikazu Yamada* of Hiroshima University. First of all, I would like to thank them for fruitful discussions, valuable advise, and kind help. Especially the practical calculation of perturbative coefficients was largely due to *K-I. Ishikawa*.

Numerical simulations were carried out on Intel Paragon XP/S at INSAM (Institute for Numerical Simulations and Applied Mathematics) in Hiroshima University. I am grateful *Shinji Hioki* (now of Tezukayama university) and *Yasuyuki Iwase* for continual support on the computational environment. I also thank *Eiji Sugiura* for his kind management of our local computer system.

S. Hioki also allowed us to use his program to generate gauge configurations. My Colleagues, *Nobuo Sasaki* and *Takashi Umeda*, kindly helped me so that I could continue the simulation even when I was absent in the University. I am grateful *Professor Minoru Yonezawa*, *Miho Kubokawa* and all members of *Hadron Physics Laboratory* for their continual support and encouragement.

I thank *Shin-ichi Tominaga* of KEK and other members of JLQCD Collaboration for useful discussions.

This research was supported in part by a grant from the Japan Society for the Promotion of Science for Young Scientists.

Finally, I wish to express my sincere gratitude to *Professor Osamu Miyamura* of Hiroshima University for his constant encouragement and for reading the manuscript and making a number of helpful suggestions.

References

[1] N. Cabibbo, Phys. Rev. **D10** (1963) 531.

[2] M. Kobayashi and T. Maskawa, Prog. Theor. Phys. **49** (1973) 652.

[3] For a review, J.L. Rosner, Nucl. Phys. B (Proc. Suppl.) **59** (1997) 1.

[4] For current status report, see *e.g.* J.Y. Seeman, Nucl. Phys. B (Proc. Suppl.) **59** (1997) 51; M. Hazumi, it ibid., 61.

[5] J.P. Alexander *et al.* (CLEO Collaboration), Phys. Rev. Lett. **77** (1996) 5000.

[6] For a review, M. Neubert, Phys. Rep. **245** (1994) 259.

[7] N. Isgur and M.B. Wise, Phys. Rev. **D42** (1994) 2388

[8] H. Georgi, Lectures delivered at TASI, Published in Boulder TASI 91, 589 (HUTP-91-A039).

[9] G. Burdman and J.F. Donoghue, Phys. Lett. **B280** (1992) 287; M.B. Wise, Phys. Rev. **D45** (1992) R2188.

[10] N. Kitazawa and T. Kurimoto, Phys. Lett. **B323** (1994) 65.

[11] G. Burdman, Z. Ligeti, M. Neubert and Y. Nir, Phys. Rev. **D49** (1994) 2331.

[12] J.N. Simone, Nucl. Phys. B (Proc. Suppl.) **47** (1996) 17.

[13] J. Flynn, Nucl. Phys. B (Proc. Suppl.) **53** (1997) 168.

[14] T. Onogi, Nucl. Phys. B (Proc. Suppl.) **63** (1998) 59.

[15] A. Abada *et al.*, Nucl. Phys. **B416** (1994) 675.

[16] C.R. Allton *et al.* (APE Collaboration), Phys. Lett. **B345** (1995) 513.

[17] A. Abada *et al.*, (APE Collaboration), Phys. Lett. **B365** (1996) 275.

[18] T. Battacharya and R. Gupta, Nucl.Phys. B (Proc. Suppl.) **42** (1995) 935.

[19] K.C. Bowler *et al.* (UKQCD Collaboration), Phys. Rev. Lett. **72** (1994) 1398; *ibid*, Phys. Rev. **D51** (1995) 4955.

[20] D.R. Burford *et al.* (UKQCD Collaboration), Nucl. Phys. **B447** (1995) 425.

[21] J.M. Flynn *et al.* (UKQCD Collaboration), Nucl. Phys. **B461** (1996) 327; J.M. Flynn and J. Nieves (UKQCD Collaboration), Nucl. Phys. **B476** (1996) 313.

[22] G. Güsken, K. Schilling and G. Siegert, Nucl.Phys. B (Proc. Suppl.) **53** (1996) 485.

[23] S. Aoki *et al.* (JLQCD Collaboration), Nucl. Phys. B (Proc. Suppl.) **63** (1998) 380.

[24] B.A. Thacker and G.P. Lepage, Phys. Rev. **D43** (1991) 196; G.P. Lepage *et al.*, Phys. Rev. **D46** (1992) 4052.

[25] C.T.H. Davies and B.A. Thacker, Phys. Rev. **D45** (1992) 915;

[26] C.T.H. Davies and B.A. Thacker, Phys. Rev. **D48** (1993) 1329;

[27] C.J. Morningstar, Phys. Rev. **D48** (1993) 2265;

[28] For a review, see J. Shigemitsu, Nucl. Phys. B (Proc. Suppl.) **53** (1997) 16.

[29] For a review, see A. Ali Khan, Nucl. Phys. B (Proc. Suppl.) **63** (1998) 71.

[30] K.-I. Ishikawa *et al.*, Phys. Rev. **D56** (1997) 7028.

[31] K.-I. Ishikawa *et al.*, Nucl. Phys. B (Proc. Suppl.) **63** (1998) 344.

[32] A. Ali Khan *et al.*, Phys. Rev. **D56** (1997) 7012.

[33] J. Shigemitsu, Nucl. Phys. B (Proc. Suppl.) **60A** (1998) 134.

[34] See *e.g.* H.J. Rothe, '*LATTICE GAUGE TEORIES: An Introduction, 2nd ed.*', World Scientific (1997), Singapore.

[35] A.X. El-Khadra, A.S. Kronfeld, and P.B. Mackenzie, Phys. Rev. **D55** (1997) 3933.

[36] G.P. Lepage and P.B. Mackenzie, Phys. Rev. **D48** (1993) 2250.

[37] G.P. Lepage, Nucl. Phys. B (Proc. Suppl.) **26** (1992) 45.

[38] N. Cabibbo and E. Marinari, Phys. Lett. **B119** (1982) 387.

[39] R. Gupta *et al.*, Phys. Rev. **D36** (1987) 2813.

[40] H.A. van der Vorst, SIAM J. Sci. Stat. Comput. 13 (1992) 631.

[41] Y. Oyanagi, Comp. Phys. Comm. 42 (1986) 333.